AD-A265 352

‖‖‖‖‖‖‖‖‖‖‖‖‖‖

CORROSION BEHAVIOR OF
METAL MATRIX COMPOSITES

FINAL REPORT FOR THE PERIOD
July 1, 1989 through September 1992

CONTRACT NO. ?.J0014-89-J-3116

Principal Investigator

Harovel G. Wheat
Mechanical Engineering
Center for Materials Science and Engineering
The University of Texas at Austin
Austin, TX 78712

S DTIC
ELECTE
MAY 2 8 1993
E D

JANUARY 1993

93-12493
‖‖‖‖‖‖‖‖‖‖‖‖‖‖

93 ○ ○ ○ ○ 4

REPORT DOCUMENTATION PAGE

Form Approved
OMB No 0704 0188

1a REPORT SECURITY CLASSIFICATION	1b RESTRICTIVE MARKINGS
Unclassified	
2a SECURITY CLASSIFICATION AUTHORITY	3 DISTRIBUTION / AVAILABILITY OF REPORT
2b DECLASSIFICATION / DOWNGRADING SCHEDULE	
4 PERFORMING ORGANIZATION REPORT NUMBER(S)	5 MONITORING ORGANIZATION REPORT NUMBER(S)

6a NAME OF PERFORMING ORGANIZATION	6b OFFICE SYMBOL (If applicable)	7a NAME OF MONITORING ORGANIZATION
The University of Texas at Austin		Office of Naval Research
6c ADDRESS (City, State, and ZIP Code)		7b ADDRESS (City, State, and ZIP Code)
Mechanical Engineering The University of Texas at Austin Austin, TX 78712		800 N. Quincy Street Arlington, VA 22217-5000

8a NAME OF FUNDING / SPONSORING ORGANIZATION	8b OFFICE SYMBOL (If applicable)	9 PROCUREMENT INSTRUMENT IDENTIFICATION NUMBER
Office of Naval Research		

8c ADDRESS (City, State, and ZIP Code)	10 SOURCE OF FUNDING NUMBERS			
	PROGRAM ELEMENT NO	PROJECT NO	TASK NO	WORK UNIT ACCESSION NO
Arlington, VA 22217-5000	89-J-3116			

11 TITLE (Include Security Classification)

Corrosion Behavior of Metal Matrix Composites

12 PERSONAL AUTHOR(S)
H. Sun, J.E. Orth, and H.G. Wheat

13a TYPE OF REPORT	13b TIME COVERED	14 DATE OF REPORT (Year, Month, Day)	15 PAGE COUNT
Final Report	FROM 7/1/89 TO 9/30/92	1993/Jan/29	78

16 SUPPLEMENTARY NOTATION

17 COSATI CODES			18 SUBJECT TERMS (Continue on reverse if necessary and identify by block number)
FIELD	GROUP	SUB-GROUP	Corrosion, Copper Metal Matrix Composites, Graphite, Dispersion Strengthened Copper

19 ABSTRACT (Continue on reverse if necessary and identify by block number)

A research program was conducted to assess the corrosion behavior of two categories of copper metal matrix composites; commercially available composites and composites in development. The commercially available composite studied was dispersion strengthened copper (2.7 vol% Al_2O_3/Cu) which was found to possess comparable corrosion resistance to copper. In addition, it did not appear to be susceptible to stress corrosion cracking when U-bend specimens were tested in 3.5 wt % NaCl or artificial seawater for a period of 4 months. Stress corrosion cracking was also not observed under proof ring loading in 3.5 wt % NaCl for a period of 8 months at an applied stress of 95% of the yield stress.

The composites in development studied were HEHR Gr_p/Cu composites containing 1.2, 5, 15, 25 and 40 vol % graphite; 50 vol % Gr_f/Cu; and 70 vol % W_f/Cu. These composites experienced varying degrees of galvanic corrosion during polarization. Benzotriazole, however, offers excellent potential as a corrosion inhibitor for these composites.

20 DISTRIBUTION / AVAILABILITY OF ABSTRACT	21 ABSTRACT SECURITY CLASSIFICATION
☒ UNCLASSIFIED/UNLIMITED ☐ SAME AS RPT ☐ DTIC USERS	Unrestricted
22a NAME OF RESPONSIBLE INDIVIDUAL	22b TELEPHONE (Include Area Code)	22c OFFICE SYMBOL
A. J. Sedriks	(202) 696-4401	1131 M

DD Form 1473, JUN 86
Previous editions are obsolete
SECURITY CLASSIFICATION OF THIS PAGE

1. INTRODUCTION

Metal matrix composites (MMCs) basically consist of a reinforcement incorporated into a metallic matrix. By adding elemental, metallic or ceramic reinforcements in various forms, including whiskers, particulates, and fibers to a metal matrix, a composite material is created that may possess superior properties over the monolithic material. In fact, the most important reason to develop MMCs is that they can be tailored to meet the critical performance requirements for advanced engineering applications. These requirements include high strength and stiffness, low densities, and low coefficients of thermal expansion. Although the incorporation of the second phase into a matrix material can enhance the physical and mechanical properties of that material, it could also significantly change the corrosion behavior (1, 2). Composites, by their nature, combine materials having considerably different corrosion properties. With regard to corrosion resistance, the dual natures of metal matrix composites make them susceptible to three adverse processes (3); localized galvanic corrosion due to coupling of the metal and reinforcement; crevice attack at the metal/reinforcement interface; and preferred localized attack at structural and compositional inhomogeneities within the metal matrix.

The work described in this report focuses on aluminum metal matrix composites and copper metal matrix composites. The work on SiC/6061 Al has been published (2) and is not included in this report. The work on the effect of thermal history on the corrosion behavior of Gr/Al is not complete and will be presented at the Corrosion/93 Poster Session sponsored by the National Association of Corrosion Engineers (4).

There is increasing interest in the utilization of Cu metal matrix composites for marine applications. Unfortunately, very limited corrosion studies of Cu metal matrix composites in chloride environments have been performed to date (5).

The primary goal of this research has been to understand the corrosion behavior of metal matrix composites in neutral chloride solutions. In particular, the effects of dissolved oxygen on the reduction and oxidation kinetics, the effect of type and form of reinforcement, and the effect

1

of increasing the volume fraction of reinforcement have been investigated. Particular attention has been given to the corrosion morphology, the corrosion mechanisms involved, and the corrosion susceptibility of the copper composites.

The corrosion behavior of copper metal matrix composites that are either commercially available or in development was studied in neutral open to air, aerated and deaerated 3.5 wt% sodium chloride solutions using electrochemical techniques, scanning electron microscopy (SEM), energy dispersive x-ray spectroscopy (EDX), and in some cases a rotating disk electrode, U-bend specimens, proof ring loading, corrosion inhibitors, ionic solution analysis and Auger electron spectroscopy (AES). The materials under investigation were dispersion strengthened copper (Al_2O_3/Cu or DSCu); high energy-high rate (HEHR) consolidated particulate graphite reinforced copper metal matrix composites consisting of 1.2, 5, 15, 25, and 40 vol% graphite; 50 vol% ± 30° angle-plied continuous P100 graphite fiber copper metal matrix composites; and 70 vol% unidirectional continuous type 218-CS tungsten wire reinforced copper metal matrix composites. Electrochemical techniques were used to determine the effects of chloride on the corrosion behavior of the various composites.

Distribution /

Availability Codes

Dist	Avail and / or Special
A-1	

2. MATERIALS

2.1 Commercially Available Composites

2.1.1 Dispersion Strengthened (DS) Copper

The DS copper was obtained from SCM Metal Products, Inc. DS Cu is produced from a blend of pure copper and aluminum powders and the finely distributed (2.7 vol% Al_2O_3) particles are achieved by an internal oxidation process. Properties for DS Cu are given in Table 1. The properties are quite impressive. In fact, in a report to Naval Sea Systems Command, Aylor (4) indicated that of the following materials Al_2O_3/Cu, TiC/Cu, Si_3N_4/Cu, Si/Cu, B_4/Cu and Gr/Cu, dispersion-strengthened (DS) copper or (Al_2O_3/Cu) was the most promising material for high-strength marine applications. In addition, the material's sea water corrosion behavior in

low flow conditions was similar to that of pure copper, while the mechanical properties and modules were significantly increased over pure copper.

2.2 Composites In Development

2.2.1 Particulate Graphite Reinforced Copper MMCs

The particulate graphite reinforced copper metal matrix composites were fabricated at the Center for Electromagnetics at The University of Texas at Austin. High energy-high rate (HEHR) consolidation techniques were utilized in this process. This process involves the internal heating of a composite powder blend through the rapid discharge of a homopolar generator (HPG). Details on the pulsed homopolar generator used in this novel processing technique and information on the tribological properties of these composites are discussed elsewhere (7,8). HEHR processing employs a 10 Megajoule homopolar generator that supplies a 100 kiloamp pulse to rapidly heat and solidify the composite powder compact. This short time at high temperature and the preferential heating and melting at the graphite-copper interface serve to encapsulate the graphite reinforcement, thereby providing a highly dense composite product. A schematic detailing the HEHR consolidation assembly is shown in Figure 1 and a typical HPG consolidation pulse shape is shown in Figure 2. An in depth discussion on the fundamental approaches to high energy-high rate processing has been described by Marcus et al, (9).

The Gr_p/Cu composites are processed in the following manner. A ceramic coating of boron nitride is sprayed onto the electrodes, die, and backing ring contact surfaces to prevent arcing during processing. The composite powder blend is loaded into a cold wall die made from seamless stainless steel hydraulic tubing. The powder blend which is contained by electrodes in the top and bottom, is compacted with the desired pressure (275 MPa for these specimens). The HPG discharges a 100 kiloAmp pulse in 200 milliseconds to consolidate t he compact via internal heating and welding of the powder particles. The pressure is maintained for five minutes to permit conductive heat transfer through the electrodes to the large copper platens. The die is unloaded and the consolidated Gr_p/Cu product removed. These processing parameters have been

developed and refined to optimize the tribological properties of these binderless Gr$_p$/Cu composites.

Particulate reinforced graphite copper metal matrix composites are currently used as sliding electrical contacts for generator parts in the automotive, utility, and aerospace industries (10). Sliding electrical contacts transfer current between stationary and moving parts of electrical machinery. Commercially available brushes incorporate low temperature binders such as lead or tin to improve the strength and interfacial bonding of the brush material. These binders decrease the conductivity of the electrical contact and tend to melt in high velocity-high current applications, resulting in decreased conductivity and excessive wear of the electrical contact. Sliding electrical contacts for high velocity-high current applications must demonstrate high conductivity and wear resistance at high sliding interface temperatures (11). Therefore, binderless graphite reinforced copper composites offer an attractive alternative for high velocity-high current applications.

The composites studied were manufactured using dendritic copper powders (325 mesh) and graphite flakes (230 mesh). Dendritic copper powders are used over spherical powders because the dendritic powders increase the interfacial contact between the copper and the graphite reinforcement. This increase in interfacial contact provides a more highly dense microstructure due to more efficient and thorough interfacial heating. HEHR consolidation techniques were utilized to fabricate 1.2, 5, 15, 25, and 40 volume percent Gr$_p$/Cu composites; HEHR consolidated dendritic copper, conventionally processed powder metallurgy (P/M) copper, and electrolytic tough pitch (ETP) copper specimens were also included in this study as control specimens.. All specimens, with the exception of the ETP samples, were pressed at 275 MPa during their respective processing techniques and manufactured as circular coupons 22 mm in diameter. ETP copper was obtained from Farmers Copper.

4

2.2.2 Graphite Fiber Reinforced Copper MMCs

The angle-plied continuous fiber reinforced graphite/copper MMCs studied in this project were manufactured at NASA Lewis Research Center in Cleveland, OH. All Grf/Cu composites tested were manufactured using pitch based P-100 graphite fibers, 10 μm in diameter, produced by Amoco Performance Products.

Currently, processing and manufacturing of these composites is labor intensive. The graphite fibers are cut from a spool and manually spread and positioned with a scalpel to insure proper alignment. Commercially available Cu coated P-100 graphite fibers from American Cyanamide Co. are utilized to manufacture the Grf/Cu composites. Liquid infiltration techniques are used in this process. Essentially, copper coated graphite yarns are hand cut from a spool, soaked in water, examined for defects, and manually positioned within an open-ended die. Proper alignment and distribution of the fibers is essential. Multilayer, angle-plied or unidirectional composites are manufactured in this manner simply by placing and orienting layers of yarns appropriately. The resulting sandwich structure is placed in a vacuum furnace and heated to 399°K until the water has boiled and the pressure reaches 10^{-5} torr. The fiber sandwich is then consolidated into the finished composite panel by hot pressing in an argon-3.75 % hydrogen atmosphere. The complete details of this consolidation technique and mechanical and thermal properties are given by McDanels and Diaz (12). The excellent specific thermal conductivity, high modulus of elasticity, and high tensile strength make Grf/Cu composites ideal candidates for high heat flux structures such as space power radiator panels where component density is a critical concern.

2.2.3 Tungsten Fiber Reinforced Copper MMCs

The unidirectional continuous fiber reinforced tungsten/copper MMCs studied in this project were also manufactured at NASA Lewis Research Center in Cleveland, OH. Commercially available Type 218CS tungsten filament wire from General Electric Corp., 180 μm in diameter, was used as the reinforcement.   Oxygen free, high conductivity copper (99.994% Cu) was selected as the matrix material for the following reasons: it has a

melting point below the recrystallization temperature of tungsten, copper is insoluble in tungsten (13) and molten copper wets tungsten (14).

The W_f/Cu MMCs were manufactured using liquid phase infiltration techniques. Continuous unidirectional tungsten fibers were placed in ceramic tubes to assure axial orientation and infiltrated with copper. Clean slugs of copper were placed above the tungsten fiber bundles. The ceramic tube and its contents were placed in a vacuum of a hydrogen furnace and heated at 1478°K for one hour. The copper melted and flowed over and around the tungsten wires to form a sound, dense MMC. After this time, the specimen rods were removed from the ceramic tubes and stored in a dessicator. Details of this process and the mechanical properties of these composites are discussed by McDanels et al (15,16). The ease of manufacturing these composites allowed for the mechanical properties to be investigated over a wide range of volume percent reinforcement. A 70vol% W_f/Cu MMC was studied in particular.

Tungsten reinforced composites are ideal for high strength, high thermal conductivity applications where component weight is not a limiting criteria. The density of tungsten is 19.26 g/cm^3, resulting in a composite density of 16.16 g/cm^3 for a 70vol% W_f/Cu MMC. Due to the high strength and conductivity of these composites, they offer potential as components in high temperature aircraft and rocket engine turbines.

2.3 Microstructural Properties of MMCs

The nature of any surface prior to any electrochemical testing must be understood and characterized in order to determine the types of corrosion initiation sites present. In particular, the reinforcement/matrix interface must be examined to evaluate it as a potential initiation site for localized galvanic corrosion or crevice corrosion. Variations in the surface can also affect the continuity and integrity of a protective film and promote increased localized attack. Structural flaws from processing, such as crevices or pores, can also result in increased localized corrosion. These structural flaws can result from the incomplete wetting of the reinforcement by the molten copper during processing and tend to create differential aeration cells, thus enhancing localized

6

corrosion. Considering these possibilities, the microstructural properties of copper MMCs must be identified at the onset of corrosion testing.

Figures 3 through 6 show micrographs of ETP copper or the copper composites prior to electrochemical testing. (The micrograph of ETP Cu is included for comparison.)

2.3.1 ETP Cu

Figure 3 shows an SEM micrographs of the Cu surface prior to electrochemical testing.

2.3.2 Dispersion Strengthened (DS) Copper

A representative as-polished microstructure of DS Cu prior to electrochemical testing is shown in Figure 4a. Dilute nitric acid solution was used to etch the polished DS Cu sample surface to reveal the particles shown in Figure 4b.

2.3.3 Gr$_p$/Cu MMCs

A representative as-polished microstructure of one of the graphite particulate reinforced copper composites, a 25 vol% Grp/Cu composite, prior to electrochemical testing is shown in Figure 5a. The samples displays relatively uniform distribution of the graphite particles in the copper matrix although graphite pullout resulting from metallurgical preparation is evident. The dark areas in this figure are graphite particles and the brighter areas that are rough in appearance are surface defects due to graphite pullout. Black areas at the graphite-copper interface are voids where the molten copper did not completely wet the graphite reinforcement. These surface defects and voids may set up differential aeration cells and act as preferential initiation sites for localized corrosion.

The nature of the graphite-copper interface was investigated by heavily etching virgin specimens in 50% NH$_4$OH + 50% H$_2$O$_2$. An SEM micrograph of such a heavily etched 25 vol% Grp/Cu composite in shown in Figure 5b. Note the good mechanical bonding at the interface. This microencapsulation of the graphite flake results from the rapid heating and cooling of the copper matrix during HEHR processing. Tight microencapsulation of the graphite particle leads to a more dense composite and provides fewer preferential anodic sites to participate in localized corrosion processes. The as-processed residual porosity measurements for all Grp/Cu HEHR

consolidated composites and P/M (powder metallurgically prepared) copper control specimens are given in Table 2. These values are averages of measurements performed on at least three different specimens using the water displacement method. All HEHR consolidated Gr_f/Cu composites have less residual porosity than their P/M processed counterparts.

2.3.4 Gr_f/Cu MMCs

A representative as-polished, unetched microstructure of a 50 vol% Gr_f/Cu composite prior to electrochemical testing is shown in Figure 6. Note the uniform fiber distribution throughout the panel, although a few areas of fiber clusters and strings of touching are observed. The grain structure and the nature of the fiber-matrix interface were examined. Fiber-matrix debonding does not occur. A sound, fully dense composite results from these consolidation techniques.

2.3.5 W_f/Cu MMCs

A typical cross section of an as-polished unetched W_f/Cu composite is shown in Figure 7. The fibers are properly oriented and evenly distributed throughout the copper matrix. A few regions of incomplete penetration of the molten copper into the tungsten tows were noted. These areas may act as initiation sites for localized corrosion. The interface is sound and voids are not observed.

3. EXPERIMENTAL PROCEDURE

All electrochemical tests were conducted on planar electrodes using an EG&G Model 273 Potentiostat/Galvanostat, EG&G model 342 software, a five mouth flask, and a flat specimen holder. The specimen holder exposed a 1.0 cm^2 surface area unless otherwise noted. For example, in the case of the HEHR composites, the five mouth flask and flat specimen holder were specially designed and manufactured to accommodate the 22 mm diameter of the HEHR composite specimens. Potentials were measured using a saturated calomel electrode (SCE) with a Luggin capillary equipped with a Vycor fitted tip. The tip was located approximately 1 mm from the exposed specimen. Two graphite counter electrodes were used to assure current symmetry.

Electrochemical tests were conducted in open to air, aerated and deaerated 3.5 wt% NaCl solutions prepared prior to each test using reagent grade sodium chloride and distilled water (pH 7.0 ± 0.2) Solutions were aerated or deaerated by sparging the solution for a period of 1 hour preceding and during the test by using industrial grade oxygen or nitrogen, respectively. Typical values of the dissolved oxygen concentration in aerated solutions were 10 ppm, whereas the concentration in deaerated solutions was between 0.5 and 1.4 ppm.

Additional electrode preparation techniques are discussed in the particular subsection if specimen geometry dictated special mounting techniques and electrical connections. Any modifications required on the test equipment during testing are also discussed. In general, all electrodes were sequentially polished from 180 to 600 grit surface finishes using SiC paper and distilled water as the lubricant. The DS Cu samp¹ s were subsequently polished with alumina powder. Specimens were rinsed in distilled water for 20 seconds, dried with a burst of laboratory air, and placed in a dessicator for storage.

Open circuit potentials were monitored as a function of time for all specimens. The steady state corrosion potentials were designated as E_{corr}. Average E_{corr} values were determined from the results of at least three runs on separate samples. It was found that between 2 and 5 hours were required for samples to reach steady state E_{corr} values in the solutions. Therefore, the samples were immersed in the solution for between 2 and 5 hours before beginning the tests. At the end of E_{corr} vs. time tests, samples were examined using SEM. Specific times will be noted for the particular composite. During subsequent electrochemical tests, specimens were allowed to reach stable E_{corr} values prior to conducting the particular electrochemical test. The corrosion behavior of the copper control samples and the copper MMCs was determined using electrochemical techniques such as potentiodynamic polariz . ion, anodic and cathodic Tafel plots, linear polarization, and in some cases, potentiostatic polarization techniques. Other techniques such as the use of the rotating disk electrode, will be described in the different subsections. Linear polarization techniques were conducted at a scan rate of 0.1 mV/sec and 0.2 mV/sec, anodic and cathodic Tafel plots were conducted at a scan rate of 0.1 mV/sec and 0.2

mV/sec, and potentiodynamic polarization tests were performed at scan rate of between 0.1, 0.2 and 1 mV/sec. Specific scan rates will be noted.

The susceptibility to stress corrosion cracking of DS Cu was examined using U-bend specimens and proof ring loading and the effectiveness of corrosion inhibitors such as benzotriazole was examined for the Gr_p, Gr_f and W_f/copper composites. The specific procedures will be described in the appropriate sections.

4. RESULTS AND DISCUSSION

4.1 Pure Copper

The open circuit corrosion potentials of the ETP Cu specimens approached a steady state value in approximately 2 hours, with the values being -0.204 V vs SCE in aerated 3.5% NaCl and -0.290 V vs SCE in deaerated 3.5% NaCl. As expected, the E_{corr} values are more active in the deaerated solution. This electronegative shift results from the inability of the electrode surface to form a continuous protective oxide layer; insufficient dissolved oxygen is present in the deaerated solutions to form such an oxide film.

SEM micrographs of the ETP Cu after 6 hours immersion in aerated and deaerated 3.5% NaCl solutions are shown in Figures 8a and 8b. SEM micrographs of the HEHR Cu after immersion under aerated and deaerated conditions are shown in Figures 9a and 9b for comparison. EDX spectra revealed that only trace amounts of chlorine were found on the electrode surfaces, regardless of the dissolved oxygen concentration.

Typical potentiodynamic polarization behavior of ETP Cu is shown in Figures 10a and 10b. Scan rates were 1m v/sec. The polarization curve is divided into four regions of behavior: 1) the apparent Tafel region; 2) the peak current and minimum current region; 3) the limiting current region; and 4) the post-limiting current higher potential region. (It should be pointed out that region 4 is not as steep at slower scan rates.) This is consistent with the behavior of pure copper in chloride media as detailed by Lee and Nobe (17) and Milosev and Metikos-Hukovic (18). The anodic polarization behavior is dependent on the mass transport reaction mechanisms

10

of the chloride ions. A model to explain the anodic polarization characteristics of Cu has been proposed (19) and is described below. Considering the anodic reaction in chloride media

$$Cu + Cl^- = CuCl^- + e^- \qquad (1)$$

$$CuCl^- + Cl^- = CuCl^-_2 \qquad (2)$$
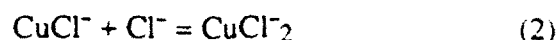
the corrosion process involves at least three steps: (a) transport of chloride ions to the Cu/NaCl solution interface, (b) reactions (1) and (2) at the interface, and (c) transport of the corrosion products away from the interface or deposition of the products on the Cu surface. Each of these reactions has its own rate-limiting step. At the lower applied potentials of region 1, the rate of formation of the CuCl is slow in comparison to the transport rate to the interface of the Cl⁻ and the rate of CuCl dissolution, equation (2). In this region, the CuCl is dissolved during the corrosion process and the corrosion behavior is limited by the reaction rate in equation (1). As higher potentials are reached in region 2, the rate of CuCl formation increases due to its dependence on potential. Excess CuCl builds up on the surface of the copper when the rate of CuCl formation surpasses its dissolution rate, equation (2). This hinders the transport of Cl⁻ to the surface. The transport of Cl⁻ becomes the rate limiting process at the peak current in region 2. As it becomes more difficult for the Cl⁻ to reach the metal surface, the rate of CuCl formation decreases while the dissolution of the CuCl continues at a rate that is independent of its film thickness. This results in the limiting current behavior observed in region 3. At even higher potentials, the rates of CuCl formation and dissolution become equal, resulting in region 4 behavior. Here the film thickness, CuCl formation and dissolution rates, and the current in this region become constant.

4.2 Commercially Available Composites

4.2.1 Dispersion Strengthened Copper

4.2.1.1 Behavior at E_{corr}

Scanning electron micrographs that were obtained after E_{corr} vs. time (6 hours) experiments are shown in Figures 11a and 11b. All cases seem to indicate the presence of a surface film which appears to be evenly distributed over the surface.

In the case of DS Cu, it was found that about 5 hours were required for samples to reach steady state E_{corr} values in the solution. Therefore, the samples were immersed in the solution for 5 hours before beginning the tests.

4.2.1.2 Polarization Tests

In the potentiodynamic tests, scanning ranges were set from E_{corr} or -250 mV below E_{corr} to +800 mV vs. SCE and +250 mV above E_{corr} or E_{corr} to -1500 mV vs. SCE for anodic and cathodic polarization, respectively. Tests were run at a scan rate of 0.1 and 1 mV/sec.

In subsequent experiments, potentiostatic tests were performed to determine the current vs. time behavior of DS Cu in deaerated and aerated solution at applied potentials of -200, -80, 0, 200, and 600 mV vs. SCE.

SEM studies were performed both before and after electrochemical testing for ETP Cu and DS Cu samples. X-ray diffraction and ICP-AES techniques were used to study the corrosion products to reveal the corrosion mechanism involved.

The shapes of the polarization curves were almost identical for ETP Cu and DS Cu under all test conditions. Typical anodic polarization curves (determined at a scan rate of 1mV/sec) for DS Cu are shown in Figures 12a and 12b. In the potential range examined, there are again four distinct regions: the apparent Tafel region (1), the peak current region (2), current minimum region (3), and the higher potential region (4). This is similar to results observed by Lee and Nobe (17). These four regions appeared in the test started from E_{corr} to +800 mV and -250 mV below E_{corr} to +800 mV. Under the aerated condition, a secondary peak current appeared in region 4, as seen in Figure 12b.

By carefully examining the polarization curves for both DS Cu and pure Cu, it is found that in deaerated solutions the average transition potential of region 4 is slightly higher for DS Cu (170mV vs SCE) than that for pure Cu (160mV vs SCE), as listed in Table 3. This can be understood from the model discussed in the section on pure Cu. The transition potential of the region 4 corresponds to initiation of the balance between the rates of CuCl formation and dissolution. Compared to pure Cu, as shown in Figures 13 and 14, the corrosion surfaces of DS

12

Cu samples are more rough due to the dispersed fine alumina particles. The alumina particles on the corroded sample surface make it difficult to cover the surface with CuCl film. In other words, a thicker film is required to cover the surface to the extent of the smooth pure surface, which means higher potential is required for the DS Cu to reach the region 4.

Table 3 also indicates that the transition potentials of region 4 for both Cu and DS Cu are higher in aerated solutions than that in deaerated chloride solutions. In chloride media containing dissolved oxygen, the electroreduction of the oxygen shifts the equilibrium of the $CuCl_2^-$ reaction (combination of equation (1) and (2)):

$$Cu + 2CuCl^- = CuCl_2^- + e \qquad (3)$$
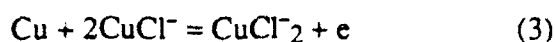
at the copper-solution interface so that a much higher interfacial concentration of $CuCl_2^-$ is obtained than in the absence of oxygen. This, then, leads to the increased dissolution rate of CuCl (equation (2)) and thus higher transition potentials are required for the balance between the formation and dissolution of the CuCl.

The typical cathodic polarization curves of Cu and DS Cu under deaerated condition are shown in Figure 15. Two cathodic peaks were observed. The second peak immediately follows the first cathodic peak. Bjorndahl and Nobe (19) suggested that the cathodic peaks were caused by CuCl reduction, equation (2), and the oxygen reduction reaction

$$O_2 + H_2O + 4e^- = 4OH^- \qquad (4)$$

4.2.1.3 Potentiostatic Tests

Potentiostatic tests were performed for 30 minutes after a 2 hour delay for both aerated and deaerated conditions. For an applied potential of -200 mV vs. SCE, which is in Tafel region, the current density oscillated between 0 and 1000 mA/cm^2; this is similar to behavior at the open circuit potential. For applied potentials of -80, 0, 200 and 600 mV vs. SCE, the current density increased to a value that depended on the applied potential and then leveled off. Under deaerated conditions, the current density oscillated between 0 and 1000 mA/cm^2 for applied potentials of -200 and -80 mV vs. SCE. The current density increases first and then leveled off for applied potentials of 0 and 200 mV vs SCE. For an applied potential of 600 mV, which is in the plateau

current region, the current oscillations occurred and the oscillating amplitude changed with time. Because the balance between the film formation and dissolution is dynamic, there is an instability in the corrosion process. It is believed that this oscillation is due to the instability of the surface film (20).

The corrosion surfaces were examined after the potentiostatic tests using SEM, X-ray and ICP-AES. Figure 16 a-d shows the SEM micrographs of the corrosion surfaces under deaerated conditions. It is clear that the corrosion is more serious at an applied potential of -80 mV vs SCE (around peak current) than other applied potentials, and the corrosion surface is more uniform and less corroded at 0 mV applied potential (around minimum current) than other applied potentials. In our sample which was subjected to an applied potential of 600 mV vs. SCE under deaerated conditions for 18 hours, the sample surface was covered by a thick film. The insoluble corrosion products on that surface were identified by x-ray diffraction right after the test and were determined to be copper chloride (CuCl).

4.2.1.4 Tafel Constants, Polarization Resistance, and Corrosion Rate

The anodic and cathodic Tafel constants, polarization resistance values, corrosion rates and E_{corr} values that were obtained for all test conditions are summarized in Table 4.

The experimental observations are the following:

1)   The polarization resistance values for pure Cu are lower than those for DS Cu under all conditions.

2)   The E_{corr} values are more active as the amount of oxygen decreases and they are slightly more active for DS Cu than those for pure Cu.

3)   The corrosion rates in aerated conditions are slightly higher than those in deaerated conditions.

4)   The polarization resistance values in aerated conditions are lower than those in deaerated conditions.

The results concerning the effect of oxygen on the corrosion behavior of Cu are consistent with the previous investigations (e.g., Bjorndaha and Nobe [19]). They measured the rotation

14

disc rate, w, in aerated and deaerated conditions and determined the polarization rate, R_p using $R_p \sim 1/w^{1/2}$). Their results indicate that the corrosion rate of copper in aerated chloride solution is higher than that in deaerated solution. This can be explained based on the model introduced in the section on pure copper.

From these observations, it seems that the DS Cu has comparable corrosion resistance to Cu. It is noted that the E_{corr} is more active for DS Cu than Cu. One possible reason for this is that the DS Cu may have a higher initial susceptibility to corrode compared to pure Cu because of the presence of Al_2O_3 particles. DS Cu may corrode in the interfacial area due to the residual stresses or galvanic corrosion between the alumina particles and the copper matrix. In other words, even though it may be easy to initiate corrosion in DS Cu, it may not necessarily have a higher corrosion rate than Cu because corrosion rates depend on the corrosion process. Therefore, DS Cu has comparable corrosion resistance to pure Cu after the protective film has formed on the surface while its E_{corr} is more active than that for Cu. This result was also observed by Aylor (5) in tests of the marine exposures for Cu and DS Cu for 1 to 7 months. The calculated corrosion rates based on the linear polarization testing showed that the corrosion rates for DS Cu were initially higher than those for pure copper during the first month, but the rates for the composites decreased to similar corrosion rates after 3.5 months.

Additional information on the corrosion behavior of DS Cu can be found in the work by Sun (21).

4.2.1.5. Anodic Polarization Using Rotating Disk Electrode

Since it is known that for Cu in chloride media, both the anodic and the cathodic partical reactions are affected by mass transport (22), a rotating disk electrode (RDE) was used to determine polarization curves as a function of rotation rate. The EG&G PAR Model 616 Rotating Disk Electrode was used to control the rotation rate and provide automatic operation of electrochemical experiments. A simple rotating disk electrode sample holder was designed and fabricated for each sample to replace the rather expensive commercial sample holders. The DS Cu samples (and ETP Cu samples for comparison) were machined into circular coupons that

were 1.6 cm in diameter and 0.32 cm thick and mounted in Bakelite in a similar way as in the preparation of metallurgical smples. A hole was drilled into the Bakelite to connect the sample to the rotating electrode electrically and mechanically, as shown in Figure 17. Note that samples could be easily screwed on or off the stainless rod of the electrode. Each sample was then sucessively ground using SiC papers followed by alumina powder polishing. They were subsequently subjected to the procedure for anodic polarization that has been described previously. In this case, however, the system was open to air and the rotation rates were 0, 1000, 3000, and 5000 rpm. The polarization curves are shown in Figure 17b-d and the polarization resistance values and corrosion rates are shown in Table 5. It is not clear at this point why there are variations between the R_p values determined in the static linear polarization test and the one performed at 0 rpm using the RDE. Perhaps the differences arise from the differences in the sample holders. This is being investigated. Polarization resistance values did decreases with rotation rate as expected.

4.2.1.6. Stress Corrosion Testing Using U-Bend Specimens

Since it is known that copper and copper alloys are susceptible to stress corrosion cracking, it was felt that stress corrosion cracking susceptibility should be examined. In order to investigate this susceptibility for DS Cu, a number of tests were run on the DS Cu using procedures outlined in ASTM G 30-79, Making and Using U-Bend Stress Corrosion Test Specimens and ASTM G37-85, Use of Mattson's Solution of pH 7.2 To Evaluate The Stress-Corrosion Cracking Susceptibility of Copper-Zinc Alloys.

Using the procedure outlined in ASTM G 30-79, eight (polished and bent) U-bend specimens were placed in a glass tank containing 3.5% NaCl and one was removed and microscopically examined for cracking every two weeks for 4 months. The U-bend specimens were bent using a 3.18 cm diameter aluminum tube and they were assembled using stainless steel, 7.62 cm bolts and nuts to induce stress and prevent springback of the legs and wire bushings and faucet washers to insulate the DS Cu from the stainless steel. The solution was covered with plastic to minimize evaporation and changed every month. Although a greenish

16

product developed on the surfaces, there was no evidence of stress corrosion cracking when the samples were observed microscopically after being cleaned in 1% H_2SO_4, followed by distilled water. The cracks that were observed immediately after exposure seemed to be confined to the surface film. A micrograph of the most highly stressed region of a U-bend specimen that was taken after 4 months exposure and subsequent cleaning is shown in Figure 18 .

A modified version of the above procedure was subsequently performed, this time using artificial seawater made with Ocean 50 Seamix manufactured by Jungle Laboratories Corporation . Two tanks were used; one tank representing stagnant conditions and one tank in which pumps were used to simulate flowing conditions. The velocity of the water under flowing conditions was approximately 0.244 m/s. U-bend specimens were placed in each tank and tensile specimens were placed on their sides in the stagnant tank only. These tensile specimens were examined to determine if there were any changes in mechanical properties due to the artificial seawater exposure. The solutions were replaced every week. Again, plastic sheets were placed over each tank and taped down to retard evaporation of the water. There were no significant changes in the mechanical properties after 4 months exposure and there was only cracking of the surface film. A micrograph of the most highly stressed region of a U-bend specimen after 4 months stagnant exposure and before cleaning is shown in Figure 19 . More details can be obtained from the work done by Whitley (23).

Additional U-bend specimens were examined according to ASTM G 37-65 under stagnant conditions. As before, no cracking was observed beneath the surface film for the 2 month period during which they were exposed.

4.2.1.7 Stress Corrosion Testing Using Proof Ring Loading

Dispersion strengthened copper was also subjected to testing using the CORTEST proof ring which was designed to permit testing of materials for H_2S service in accordance with NACE Test Standard TM 01-77. The procedure was modified to accommodate 3.5 % NaCl as the solution. The proof ring provides a sustained specimen load under a stress state of uniaxial tension. Small tensile specimens having a gauge length of 1.59 cm. and a width of 0.953 cm.

17

were machined and the device was calibrated by CORTEST. Tests were conducted at a stress of 0.95 of the yield strength for a period of 8 months without any evidence of cracking. However, on loading the sample to failure, it was observed that failure occurred outside the gauge length which indicates that there must be some design problems associated with the specimen configuration.

4.3 Composites In Development

4.3.1 Particulate Reinforced Gr_p/Cu MMCs

4.3.1.1 Behavior at E_{corr}

The open circuit corrosion potential, E_{corr} of the Gr_p/Cu electrodes changed rapidly after immersion and approached a steady state value in approximately 2 hours. This is consistent with the initial rapid formation of protection film. The galvanic series for sea water indicates reversible potentials of +0.25 V vs. SCE for graphite and -0.337 V vs. SCE for Cu. E_{corr} of graphite is therefore substantially noble to copper. Therefore, one would expect the corrosion potential of these Gr_p/Cu composites to become more noble as the volume fraction of graphite is increased. This trend holds true for the specimens and the values are shown in Table 6. It should be noted that in this case, the ETP Cu as well as the HEHR pure copper electrodes were used as controls.

Typical micrographs after E_{corr} vs. time tests for the HEHR pure copper and the 15 and 40 vol% Gr_p/Cu composites are shown in Figures 20a-f. Regions of graphite pullout are evident in the composites. However, they do not appear to have acted as preferential sites for localized corrosion. Prolonged exposure results in increased graphite pullout as indicated in Figure 21 which shows a the micrograph for the 1.2 vol% Gr_p/Cu composite that was exposed to aerated conditions for 10 hours.

18

4.3.1.2 Polarization Tests and Polarization Resistance

Typical potentiodynamic polarization curves for ETP Cu as well as 5 and 15 vol% Gr_p/Cu are shown in Figures 22a, b and c. Scan rates were 0.2 mV/sec. The curves are comparable and again the four regions of behavior are observed.

Potentiodynamic polarization tests of the 25 and 40 vol% Gr_p/Cu specimens exhibited small fluctuations in the anodic current density in the higher potential regions. This behavior, as demonstrated in Figure 23a and 23b for a 25 vol% Gr_p/Cu electrode, occurs when a portion of the composite would fall away from the sample surface, revealing an uncorroded surface to participate in the corrosion process. The uncorroded surface acted as a new anodic site, resulting in a momentary fluctuation in the current density. This phenomenon was observed in aerated and deaerated solutions for the 15, 25, and 40 vol% Gr_p/Cu electrodes. The same data from the polarization curve in Figure 23a, which is presented in a semi-log format, is plotted in linear format in Figure 23b, thus emphasizing the jumps in anodic current density due to exfoliation of the composite electrode.

The transition from region two behavior to region three behavior typically occurred within a given potential range of -70 to -50 mV vs. SCE, regardless of the volume percent of graphite reinforcement. Nonetheless, the volume percent of graphite reinforcement did alter the nature of the peak current and minimum current region. The change in current density within this region, defined as $\Delta i_{region\ 2} = i_{max} - i_{min}$, was calculated for pure copper and Gr_p/Cu electrodes in aerated and deaerated 3.5 wt% NaCl. Results are plotted as a function of graphite content in Figure 24. In aerated and deaerated solutions, the $\Delta i_{region\ 2}$ decreased with increasing graphite content. This is due to two effects. One, as the volume percent of graphite increases, there is less copper present in the electrode to participate in the expected polarization behavior of copper. Also, as the volume percent of graphite increases, the contribution of the galvanic current to the current density becomes more pronounced.

19

Examples of micrographs of a 5 and 15 vol% Gr$_p$/Cu MMCs after anodic polarization are shown in Figure 25. Note the galvanic attack at the graphite-copper interface and the uniform corrosion of the copper matrix.

Average polarization resistance values in aerated and deaerated sodium chloride for HEHR 100% Cu and selected composites are given in Table 7. Note that the polarization resistance decreases as the volume percent of graphite increases. This trend hold true in both aerated and deaerated 3.5wt% NaCl solutions.

The results obtained are summarized below:

1) HEHR processing offers an attractive alternative to conventional powder metallurgy techniques for the processing of metal matrix composites based on the following characteristics: extremely fast processing minimizes time for internal oxidation; rapid heating and cooling rates related to the high energy-high rate pulse; microencapsulation of graphite particle through preferential heating at the graphite-copper interface; and a dense product is achieved without requiring post-processing heat treatments.

2) Stable E$_{corr}$ values are more noble for Gr$_p$/Cu specimens immersed in aerated 3.5 wt% NaCl solutions than in deaerated solutions. E$_{corr}$ values become more noble as the volume percent graphite increases.

3) Voids in the composite due to graphite pullout during electrode preparation or surface defects do not act as initiation sites for localized corrosion phenomenon.

4) Negligible galvanic attack was observed in the 1.2, 5, and 15 vol% Gr$_p$/Cu composites at their rest potential. Galvanic corrosion between the graphite reinforcement and the copper matrix became more pronounced as the volume percent of graphite and the exposure time increased.

5) Cracks emanating from the graphite-copper interface were detected in composites immersed in deaerated and aerated NaCl solutions for 10 hours.

6) The potentiodynamic polarization curves generated for pure copper electrodes and Gr$_p$/Cu electrodes are similar. The four regions of polarization behavior are observed.

20

The change in magnitude of the peak current and minimum current region decreased as the volume percent of graphite increases because less copper is available to participate in the anodic reactions..

7) For a given volume percent reinforcement, the corrosion mechanisms of the HEHR composites are similar, independent of aeration or deaeration of the test solution. The severity of the corrosion of the Gr_p/Cu metal matrix composites increased with increasing graphite content.

8) All composite samples exhibited uniform corrosion and localized galvanic corrosion at the graphite-copper interface, Copper is reduced and goes into solution. Localized galvanic corrosion attacks the interface and small amount of exfoliation of the graphite reinforcement. The graphite-copper interface is degraded and small amounts of graphite fall away from the electrode surface. The majority of the graphite reinforcement remains on the surface and is held in place through the accumulation of corrosion product.

4.3.2 Fiber Reinforced Graphite/Copper Composites

The 50vol% Gr_f/Cu MMCs were manufactured in panel form, approximately 7 x 30 x 0.2 cm. Panels were cut into one centimeter wide strips. Each composite strip was then sectioned at one centimeter intervals, resulting in a final specimen size of 1 x 1 x 0.2 cm. Electrodes were prepared in the following manner. Electrical leads were spot-welded onto the backside of the copper foils of the samples. Specimens were then mounted in non-conductive epoxy with their edge exposed. Typical electrode areas were 0.2 cm^2. A coating of rubber cement was applied to where the electrical lead exited from the back of the epoxy sample mount to safeguard against any seepage of the electrolyte down the wire-epoxy interface. Electrodes were stored in a desiccator until electrochemical testing or microstructural observations. Electrochemical tests were conducted on the exposed edges of the Gr_f/Cu composite.

4.3.2.1 Behavior at E_{corr}

Graphs of the open circuit potentials over time for Gr_f/Cu electrodes in aerated and deaerated 3.5 wt% NaCl revealed that the electrodes reached stable E_{corr} values in approximately

21

1-2 hours. The average open circuit potential value for the electrode immersed in the aerated 3.5 wt% NaCl was -0.200 mV vs. SCE, approximately 60 mV more noble than the electrodes exposed in the deaerated solution. This is consistent with the results obtained for the particulate reinforced graphite/copper composites and pure copper control specimens; insufficient dissolved oxygen is present in deaerated solutions to form a continuous protective film on the electrode surface. An SEM micrograph of a Gr$_f$/Cu composite electrode after four hours immersion in deaerated NaCl is shown in Figure 24. Negligible corrosive attack has occurred; this micrograph is very similar to that of a virgin specimen. The interface shows no signs of localized galvanic corrosion and scratches on the surface from metallurgical preparation remain evident.

4.3.2.2 Polarization Tests and Polarization Resistance

Gr$_f$/Cu electrodes were potentiodynamically polarized using two electrochemical techniques: Tafel test polarization from E$_{corr}$ to E$_{corr}$ ±250 mV and potentiodynamic polarization to 800 mV vs. SCE. Reported results are for a scan rate of 0.2mV/s. The corrosion morphology of a Gr$_f$/Cu electrode after polariz. .on to E$_{corr}$ +250 mV during the Tafel test is examined in the SEM micrograph of Figure 27a. Deposition of corrosion product on local area cathodes (i.e., the exposed graphite fibers) is evident. Some cracking and grain boundary corrosion is also observed. A higher magnification micrograph, Figure 27b, is quite informative. The protrusion of the graphite fibers from the matrix is apparent; the copper matrix (the anode) has suffered from uniform corrosion, leaving the fibers intact. Degradation of the mechanical bond at the graphite-copper interface has occurred.

The polarization behavior of these composites is somewhat similar in nature to that of pure copper and quite similar to the Gr$_p$/Cu MMCs. A potentiodynamic polarization curve for a Gr$_f$/Cu electrode in deaerated 3.5 wt% NaCl is seen in Figure 28. (A similar polarization curve for an HEHR 100% Cu electrode is given for comparison.) The Tafel regions are similar to those of pure copper but the current maximum and current minimum regions are different. This is primarily due to the fact that there is only 50 vol% copper in the Gr$_f$/Cu composites. The higher potential region in the Gr$_f$/Cu electrode polarization curve in Figure 28 approaches higher values

in the current density at a faster rate than the pure copper electrodes. This is due to accelerated localized galvanic corrosion in the Gr$_f$/Cu composite.

SEM micrographs of a 50 vol% Gr$_f$/Cu composite electrode surface after potentiodynamic polarization to E$_{corr}$ +800 mV in deaerated NaCl are observed in Figures 29a and 29b. The general corrosion behavior is seen in Figure 29a and a higher magnification of the lower right hand region of this micrograph is observed in Figure 29b. Note the selective severe attacked of the copper matrix, accumulation of corrosion product on the noble graphite reinforcement, and an area of localized galvanic corrosion at the graphite fiber-copper matrix interface.

Gr$_f$/Cu electrodes were also polarized to similar potentials in aerated solutions to evaluate the effect of dissolved oxygen in the electrolyte on the corrosion behavior of these composites. The mode of attack in aerated solutions was significantly different from that observed in the deaerated electrolytes. The typical corrosion morphology of these composites in aerated 3.5 wt% NaCl is shown in Figure 30a. Cracking of the copper matrix is observed. Cracks originate at the graphite-copper interface and propagate through the matrix and run into other cracks or interfaces. The nature of the graphite fiber-copper interface was examined at higher magnifications in Figure 30b. Debonding has occurred at the fiber-matrix interfaces in the top left and top right of this Figure. The copper matrix has experienced cracking and severe uniform corrosion. The region of accelerated galvanic corrosion observed in deaerated solutions is absent.

A comparison of the anodic potentiodynamic curves for Gr$_f$/Cu electrodes in aerated and deaerated 3.5 wt% NaCl is made in Figure 31. Tafel behavior is similar; however, the transition to region 2 behavior occurs at a lower potential and a lower current density for the electrode in the aerated solution. This behavior is explained by returning to the behavior of pure copper as noted in section 4.1. As the applied potential increases in the Tafel region, the rate of CuCl formation increases due to its dependence on potential. In aerated NaCl, the electroreduction of the oxygen shifts the equilibrium of the $CuCl_2^-$ reaction. Excess CuCl builds up on the surface of

the Gr$_f$/Cu MMC when the rate of CuCl formation surpasses its dissolution rate. This hinders the transport of Cl$^-$, causing the current maximum to occur at lower applied potentials and lower current densities. The behavior in the limiting current and higher potential regions are similar but the current density is lower for the Gr$_f$/Cu MMC in the aerated electrolyte. Considering the micrographs taken $\approx$ E$_{corr}$ +800 mV in aerated and deaerated NaCl, it is suggested that the severity of the galvanic corrosion in the deaerated electrolyte results in the higher corrosion current densities.

Average polarization resistance values were 1.1kΩ/cm^2 and 2.8kΩ/cm^2 in aerated and deaerated NaCl respectively. Additional information can be found in the work by Orth (24).

4.3.3 Fiber Reinforced Tungsten/Copper Composites

W$_f$/Cu composites were manufactured in cylindrical form. Electrodes were made by sectioning the cylindrical MMC such that a smaller cylinder, approximately 1 cm in length, was generated. Electrical leads were spot-welded onto the back side of the composites. Specimens were then mounted in non-conductive epoxy with the circular electrode exposed. A coating of rubber cement was applied to where the electrical lead exited from the back of the epoxy sample mount to safeguard against any seepage of the electrolyte down the wire-epoxy interface. The prepared electrode was stored in a desiccator.

4.3.3.1 Behavior at E$_{corr}$

The W$_f$/Cu composites displayed behavior similar to the other composites at E$_{corr}$; the open circuit potential decreased as a function of time until it reached a steady state value in approximately 1^1/$_2$ hours. Average E$_{corr}$ values for the W$_f$/Cu electrodes immersed in the aerated 3.5 wt% NaCl were approximately -0.250V vs. SCE. This is appro. imately 50 mV more noble than their counterparts in the deaerated solutions. This is consistent with prior results for the copper control specimens and the copper MMCs.

4.3.3.2 Polarization Tests and Polarization Resistance

W_f/Cu electrodes were potentiodynamically polarized using two electrochemical techniques: Tafel test polarization from E_{corr} to $E_{corr} \pm 250$ mV, and potentiodynamic polarization to 800 mV vs. SCE, both at a scan rate of 0.2mV/s.

A polarization diagram for a W_f/Cu electrode in aerated 3.5 wt% NaCl is given in Figure 32. Tafel behavior is similar to that of pure copper. A decrease in the anodic current density is observed in the current maximum and current minimum region. However, the magnitude of this decrease is substantially less than in other copper MMCs. The corrosion current, at higher applied potentials, is also less than that of the copper control and Gr/Cu electrodes.

An SEM micrograph of the W_f/Cu electrode surface after polarization is given in Figure 33a. Uniform corrosion of the copper matrix is observed. However, the attack is not as severe as in the graphite copper composites. The noble tungsten reinforcement has not been damaged; scratches from metallurgical preparation remain evident. The tungsten-copper interface is examined in a higher magnification in Figure 33b. The interface has been degraded. Debonding between the tungsten fiber and copper matrix is evident. An area of localized galvanic corrosion is observed at the tungsten-copper interface. Note the deeper attack at the interface. Cracks originate at the interface and propagate towards the matrix with some cracks growing together. These cracks do not extend past the region of localized attack. Although the differences in the open circuit potential developed between copper and tungsten is small, galvanic corrosion is still a concern for these composites.

Polarization resistance values were found to be $1.1\text{k}\Omega/\text{cm}^2$ in aerated NaCl.

Additional information on the composites in development can be found in the work by Orth (24).

4.3.4 Corrosion Inhibitors for Copper Metal Matrix Composites

The stability of copper and copper alloys in neutral aerated NaCl solution depends on the nature of the corrosion product film, the constituents of this film, under certain conditions, being a mix of cuprous oxide, cuprous hydroxychloride, and cupric oxide (25). When this protection is

compromised, other means of protection must be found. Corrosion inhibitors offer excellent potential for the protection of copper MMCs. They offer protection of the composite without affecting or degrading any of the enhanced properties that make these MMCs attractive (such as high thermal conductivity and high electrical conductivity). For instance, chemical conversion and chromate coatings may offer significant protection of the copper MMC, yet these coatings are deleterious to the electrical and thermal conductivities of the copper MMCs, not to mention the environmental harm that may result from working with such coatings. Inhibitors are readily available, cost effective, and easy to use and monitor; however, corrosion inhibitors are only applicable to closed circulating systems. Corrosion inhibitors are available that are very effective in controlling corrosion of copper and copper base alloys. Many of these inhibitors may also be effective in minimizing galvanic deposition of dissolved copper onto other metals (26).

Three specific corrosion inhibitors have been identified and extensively used for the protection of copper and copper alloys: benzotriazole, totyltriazole, and mercaptobenzothiazole. All of these inhibitors depend on the formation of an adherent protective film on the metal oxide surface. Essentially, the inhibitor reacts with the metal surface to form a chemisorbed 3-dimensional barrier. The rate of film growth is rapid and reaches a self-limiting thickness within a short period of time (27).

Benzotriazole ($C_6H_4N_3H$) is considered as one of the most effective corrosion inhibitors for copper and copper alloys in severe environments(28,29). Benzotriazole reacts with copper to form a compact, chemisorbed, 3-dimensional barrier composed of polymeric multilayer film of $Cu-C_6H_4N_3$ (29,30). This section focuses on the effectiveness of benzotriazole as a corrosion inhibitor for copper metal matrix composites. In particular, the ability of benzotriazole to minimize galvanic corrosion has been investigated.

Benzotriazole has been evaluated as an inhibitor in 3.5 wt% NaCl solutions at a concentration of 0.2 g/l. The effects of benzotriazole on the corrosion behavior of Gr_p/Cu, Gr_f/Cu, and W_f/Cu were evaluated at: open circuit potential, during linear polarization, and during anodic potentiodynamic polarization. Results for each of these categories are discussed in

subsections below. HEHR 100% Cu electrodes were used ad control specimens. Special consideration is given to determining the effectiveness of benzotriazole as a corrosion inhibitor capable of controlling and limiting galvanic corrosion.

4.3.4 Behavior at E_{corr}

Benzotriazole is a corrosion inhibitor that forms a three dimensional polymer film on copper surfaces. This is a time dependent process and was monitored by measuring the open circuit potential as a function of time. As the benzotriazole chemisorbed onto the copper surfaces, the open circuit potential became more noble. Figures 34a-d contain E_{corr} vs. time curves in aerated 3.5 wt% NaCl +200 ppm benzotriazole for HEHR 100% Cu, 1.2 vol% Gr_p/Cu, 50 vol% Gr_f/Cu, and 70 vol% W_f/Cu electrodes, respectively. Steady state E_{corr} values were approximately -0.185, -0.185, -0.205 and -0.255 V vs. SCE for the HEHR 100% Cu, the 1.2 Vol% Gr_p/Cu, the 50% vol% Gr_f/Cu and the 70 vol% W_f/Cu respectively.

4.3.4.2 Polarization Tests and Polarization Resistance

Typical anodic polarization curve for an HEHR 100% Cu electrode with and without 200 ppm benzotriazole solution are observed in Figure 35. Typical anodic polarization curves for 1.2 vol% Gr_p/Cu electrodes in 3.5 wt% NaCl solutions with and without 200 ppm benzotriazole are given in Figure 36, and typical anodic potentiodynamic polarization curves obtained for the 50 vol% Gr_f/Cu MMCs in aerated 3.5 wt% NaCl with and without the benzotriazole are compared in Figure 37. The benzotriazole provides excellent protection of the composite and also acts as a superior deterrent to galvanic corrosion. From E_{corr} to 100mV vs SCE for pure Cu and from E_{corr} to 250 mV vs SCEfor the composites, , there is a reduction in the corrosion current in excess of two orders of magnitude. Region 2 polarization behavior does not occur for the 50vol% Gr_f/Cu mmc electrode in the benzotriazole solution; the corrosion inhibitor prevents the buildup and formation of $CuCl_2^-$ until potentials greater than 250 mV_{sce} are approached. This probably results from the decreased amount of copper present to participate in the corrosion process. The polarization curve for Gr_f/Cu electrode in the electrolyte containing the benzotriazole does not intersect its counterpart in the solution without the added corrosion

27

inhibitor. Galvanic corrosion is reduced by the addition of benzotriazole to the electrolyte. The corrosion morphologies of Gr_f/Cu electrodes exposed in the benzotriazole containing electrolytes and polarized to 600 mV_{sec} were analyzed using the SEM. Results indicate that the corrosion performance is improved for specimens exposed to the corrosion inhibitor. A low magnification SEM micrograph of a typical exposed surface is observed in Figure 38. Upon close examination of this micrograph, it is noted that the scratches from metallurgical sample preparation remain evident. The attack is localized in nature; it is concentrated in the regions where graphite bundles were placed in layers during processing.

Typical anodic polarization curves generated from W_f/Cu electrodes with and without benzotriazole are given in Figure 39. The benzotriazole provides a reduction in the corrosion current of only one order of magnitude up to 150 mV_{sce}. Apparently, benzotriazole does not affect tungsten and since there is only 30 vol% copper in these specimens, the protection is limited.

Polarization resistance values for the composites with and without benzotriazole are given in Table 8. All values are substantially higher for the electrodes immersed in the electrolytes containing the benzotriazole, indicating lower corrosion rates.

Benzotriazole offers excellent potential as a corrosion inhibitor for coppers MMCs. The open circuit potentials of the copper control specimens and the Gr_p/Cu MMCs became more noble when immersed in the NaCl solutions containing benzotriazole. The E_{corr} of the Gr_f/Cu and W_f/Cu composites are only slightly affected by the addition of benzotriazole. This is due to the smaller volume percent of copper in these composites. Polarization resistance values for all copper MMCs immersed in the NaCl-benzotriazole solutions increased over one order of magnitude, indicating lower corrosion rates for the composites in the NaCl solutions containing benzotriazole. The anodic polarization curves obtained in the NaCl + benzotriazole solutions demonstrated a decrease in the corrosion current of 2 to 3 orders of magnitude over substantial potential ranges. Improved performance was observed up to 200 mV_{sce} for W_f/Cu specimens.

300 mV$_{sce}$ for Gr$_p$/Cu samples, 250 mV$_{sce}$ for Gr$_f$/Cu electrodes, and 100 mV$_{sce}$ for copper control samples.

Typical anodic polarization curves comparing the electrochemical behavior of HEHR 100% copper and 1.2 vol% Gr$_p$/Cu electrodes in aerated 3.5 wt% NaCl + 200 ppm benzotriazole are given in Figure 40. Galvanic effects are noted at the higher applied potentials where the corrosion current is greater for the 1.2 vol% Gr$_p$/Cu composite. It is interesting to note that the benzotriazole offers a wider range of corrosion protection for the Gr$_p$/Cu composite than the pure copper specimen. Benzotriazole appears to minimize galvanic corrosion until higher applied potentials are reached.

The electrochemical behavior of HEHR 100% copper and 50 vol% Gr$_f$/Cu electrodes in aerated 3.5 wt% NaCl + 200 ppm benzotriazole are compared in Figure 41. This is a very interesting comparison. Note that the benzotriazole offers a wider range of corrosion protection for the 50 vol% Gr$_f$/Cu composite than it does for the pure copper specimen. Even when the driving force for corrosion is high enough to overcome the protective nature of the compact chemisorbed polymeric multilayer film of Cu-C$_6$H$_4$N$_3$, the corrosion current density is less than that of the pure cooper specimen.

As a corrosion inhibitor, benzotriazole is effective in preventing corrosive attack of the copper matrix and minimizing galvanic corrosion at the interface. It may be possible to expand the potential applications of this inhibitor by utilizing high concentration benzotriazole solutions as pre-treatment methods for copper MMCs.

5. CONCLUSIONS

A research program was conducted to assess the corrosion behavior of aluminum metal matrix composites and copper metal matrix composites. The conclusions concerning the aluminum metal matrix composites have been summarized in reference 2.

With respect to the copper metal matrix composites, two categories of composites were studied: commercially available composites and composites in development.

The commercially available composite studied was dispersion strengthened copper which was found to possess comparable corrosion resistance to copper. In addition, it did not appear to be susceptible to stress corrosion cracking when U-bend specimens were tested in 3.5wt% NaCl or artificial seawater for a period of 4 months. Stress corrosion cracking was also not observed under proof ring loading in 3.5 wt% NaCl for a period of 8 months. The applied stress was 95% of the yield stress.

The composites in development studied were HEHR Gr_p/Cu composites containing 1.2, 5, 15, 25 and 40 vol% graphite; 50 vol% Gr_f/Cu; and 70% vol% W_f/Cu.

The severity of the corrosion of the HEHR Gr_p/Cu composites increased with increasing graphite and in the presence of dissolved oxygen. In addition, all of the composites in development exhibited uniform corrosion and some localized galvanic corrosion at the reinforcement-copper interface during polarization. This localized corrosion led to cracking and exfoliation of the graphite reinforcement for the Gr_p/Cu MMCs. Cracking was also observed at the reinforcement-copper interface in the Gr_f/Cu and W_f/Cu MMCs.

Benzotriazole offers excellent potential as a corrosion inhibitor for these composites. Polarization resistance values were much greater for the specimens immersed in NaCl-benzotriazole solutions than their counterparts in 3.5 wt% NaCl only. This suggest much lower corrosion rates. Therefore the possibility of using benzotriazole as a pretreatment corrosion inhibitor for these copper metal matrix composites is proposed.

6. ACKNOWLEDGMENTS

7. REFERENCES

1. R. C. Paciej and V. S. Agurwala, Corrosion, Vol. 42, No. 12, p. 718, 1986.

2. H. Sun, E. Koo, and H. G. Wheat, Corrosion, Vol. 47, No. 10, p. 742, 1991.

3. P. P. Trzaskoma, Journal of Metals, p. 21, Dec. 1988.

4. H. Sun, Corrosion/93 Poster Session, National Association of Corrosion Engineers, New Orle .ns, LA 1993.

5. D. M. Aylor, "Development of Copper-base Metal Matrix Composites Materials," DTNSRDC/SME-85/10, David Taylor Naval Ship R&D Center, March, 1985.

6. SCM Metal Products, Inc., GlidCop, ed. SCM Metal Products, Cleveland, Ohio.

7. J. H. Gully, J. M. Weldon, and W. L. Noble, IEEE Transactions on Magnetics, Vol. 22, No. 6, p. 1623, 1985.

8. Z. Eliezer, C. Persad, M. J. Wang, and K. C. Owen, Wear, Vol. 120, p. 117, 1987.

9. H. L. Marcus, D. L. Bourell, Z. Eliezer, C. Persad, and W. F. Weldon, J Metals, Vol. 38, p. 6, 1986.

10. H. L. Marcus, W. F. Weldon, and C. Persad, Technical Report Contract No. N62269 85 C0222, The University of Texas at Austin, Austin, TX, February, 1987.

11. C. Persad and Z. Eliezer, Wear, Vol. 120, p. 117, 1987.

12. D. L. McDanels and J. O. Diaz, "Exploratory Feasibility Studies of Graphite Fiber Reinforced Copper Matrix Composites for Space Power Radiator Panels," NASA TM-102328, Lewis Research Center, Cleveland, OH, September, 1989.

13. M. Hansen, Constitution of Binary Alloys, Second Edition, McGraw-Hill, 1958,

14. C. J. Smithels, Tungsten. Its Metallurgy. Properties, and Applications, Chem. Pub. Co., 1953.

15. D. L. McDanels, R. W. Jech, and J. W. Weeton, "Stress Strain Behavior of Tungsten-Fiber Reinforced Copper Composites," NASA Technical Note D-1881, Lewis Research Center, Cleveland, OH, October, 1983.

16. D. L. McDanels, "Tungsten Fiber Reinforced Copper Matrix Composites, a Review," NASA Technical Paper 2924, Lewis Research Center, September, 1989.

17. H. Lee and K. Nobe, J. Electrochem. Soc., Vol. 133, No. 10, p. 2035 1986.

18. I. Milosev and M. Metikos-Hukovic, J. Electrochem. Soc, Vol. 138, No. 1, pp. 6, 1991.

19. W. D. Bjorndahl and K. Nobe, Corrosion, Vol. 40, No. 2, p. 82, 1984.

20. H. Lee, K. Nobe, and A. Pearlstein, J. Electrochem. Soc., Vol. 132, No. 5, p.1031, 1985.

21. H. Sun and H. G. Wheat, submitted to Journal of Materials Science.

22. S. R. Sanchez and D. J. Schiffrin, Corr. Sci., Vol. 22, p. 585, 1982.

23. G.A. Whitley, Jr., "Stress Corrosion Cracking Susceptibility of Dispersion Strengthened Copper," M. S. Thesis, The University of Texas at Austin, Austin, TX, May, 1991.

24. J. E. Orth, PhD. Dissertation, The University of Texas at Austin, May 1993.

25. R. R. North and M. J. Prior, Corr. Sci., Vol. 10, p. 197, 1970.

26. Personal communication with Dr. David Miller, Texaco Chemical Co., Austin Research Laboratories, Austin, TX, May 1992.

27. Metals Handbook, Ninth edition, Vol. 13, No. 3, ASM International, Metals Park, OH, p. 497, 1987.

28 G. Lewis, Br. Corros. J., Vol. 16, No. 3, pp. 169-79, 1981.

29. T. Notoya and G. W. Poling, Corrosion, Vol. 32, No. 6, p. 216-25, 1976.

30. T. Notoya and G. W. Poling, Corrosion, Vol. 35, No. 5, p. 193-99, 1979.

List of Tables

Table 1. Properties of DSC vs ETP Copper (6)

	Tensile Strength (KPSI)	Yield Strength (KPSI)	Elongation in 2 in. (%)	Hardness (Rockwell)	Density (lb/in³)	Modulus of Elasticity (MPSI)	Thermal Conductivity (68°F.BTU /ft.hr.°F)
DSC GlidCop AL-60 UNS C15760	75	60	13	$R_B = 81$	.318	19	186
Copper ETP UNS C11000	32	10	50	$R_F = 40$	.322	17	226

Table 2. Residual Porosity Measurements

vol% graphite	$\rho_{measured}$	$\rho_{theoretical}$	% residual porosity
P/M 100% Cu	8.05	8.96	10.2
HEHR 100% Cu	8.41	8.96	5.2
1.2	8.18	8.88	5.9
5	7.95	8.63	6.8
15	7.39	7.95	6.1
25	6.79	7.28	6.8
40	5.89	6.28	5.1

Table 3. The transition potentials of region 4 (mV vs SCE).

	DS Cu	Cu
Deaerated	170	160
Aerated	213	210

Table 4. Tafel Constant, R_p, and MPY Values for Cu and DS Cu

Conditions	Parameters		Cu	DS Cu
Aerated	Tafel (mv)	Anodic	41.49	72.57
		Cathodic	181.62	108.95
	R_p(K-OHMS cm ^{2})		4.28	6.66
	Ecorr (mv)		-204	-220
	Corrosion Rate (MPY)		1.90	1.51
Air	Tafel (mv)	Anodic	61.84	56.31
		Cathodic	115.44	101.38
	R_p(K-OHMS cm ^{2})		4.28	4.52
	Ecorr (mv)		-223	-247
	Corrosion Rate (MPY)		2.35	2.40
Deaerated	Tafel (mv)	Anodic	109.10	71.76
		Cathodic	108.18	358.19
	R_p(K-OHMS cm ^{2})		7.39	9.26
	Ecorr (mv)		-290	-298
	Corrosion Rate (MPY)		1.37	1.51

Table 5. The polarization resistance, corrosion rate, and i$_{corr}$
values for DS Cu and Cu

	rpm	0	1000	3000	5000
	R_p (k-ohms cm^2)	21.67	1.51	1.29	1.05
Cu	Corr. Rate (MPY)	0.47	6.68	7.79	9.61
	I_{corr} (μA/cm^2)	1.00	14.38	16.77	20.69
	R_p (k-ohms cm^2)	32.59	1.71	1.45	1.44
DS Cu	Corr. Rate (MPY)	0.38	5.88	6.10	7.01
	I_{corr} (μA/cm^2)	0.82	12.67	13.14	15.08

Table 6. Stable E$_{corr}$ Values in Aerated and Deaerated 3.5 wt % NaCl Solutions
(Values given in mV vs SCE)

vol% gr	Aerated Solutions	Deaerated Solutions
PM 100% Cu	-281	-291
HEHR 100% Cu	-273	-284
1.2	-238	-254
5	-232	-252
15	-220	-245
25	-217	-233
40	-199	-212

Table 7

Effect of O_2 on Polarization Resistance of Cu and Gr_p/Cu MMCs.

$(k\text{-ohm/cm}^2)$

	Aerated	Deaerated
HEHR 100% Cu	1.4	7.2
1.2 Vol% Gr_p/Cu	1.6	1.1
15Vol% Gr_p/Cu	0.6	0.6
40Vol% Gr_p/Cu	0.6	0.3

Table 8

Effect of Benzotriazole on Polarization Resistance of Cu and Cu MMCs.
$(k\text{-ohm/cm}^2)$

	Without Benzotriazole	with 200 ppm Benzotriazole
HEHR 100% Cu	1.8	15.0
1.2 Vol% Gr_p/Cu	1.6	5.1
50 Vol% Gr_f/Cu	1.2	9.7
70 Vol% W_f/Cu	1.1	14.9

List of Figures

Figure 1. A schematic detailing the HEHR consolidation assembly.

Figure 2. Typical HPG consolidation pulse shape and duration.

Figure 3. SEM micrograph of as-polished ETP Copper.
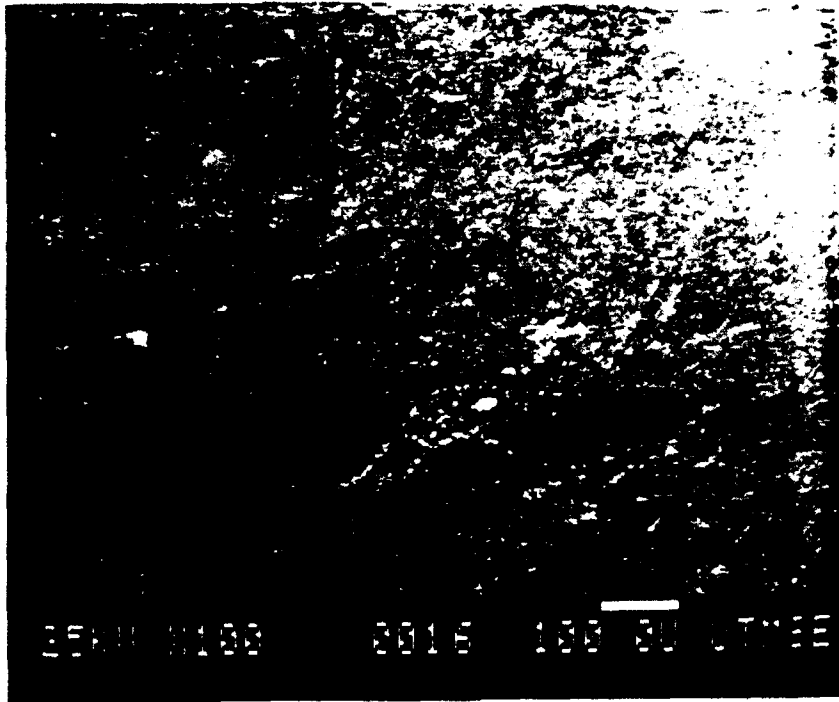
Figure 4a. SEM micrograph of as-polished DS Copper.
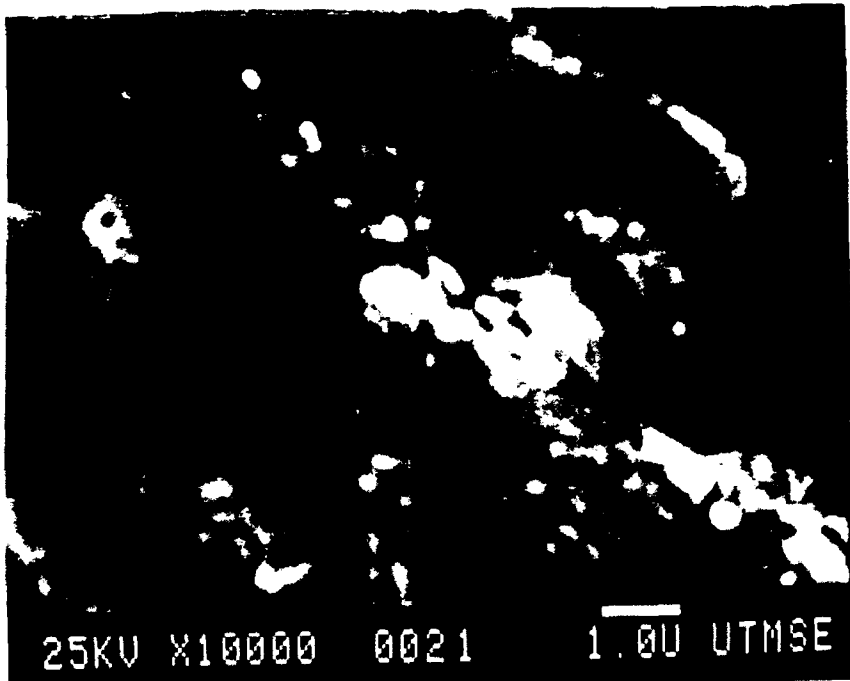
Figure 4b. SEM micrograph of polished and etched DS Copper.
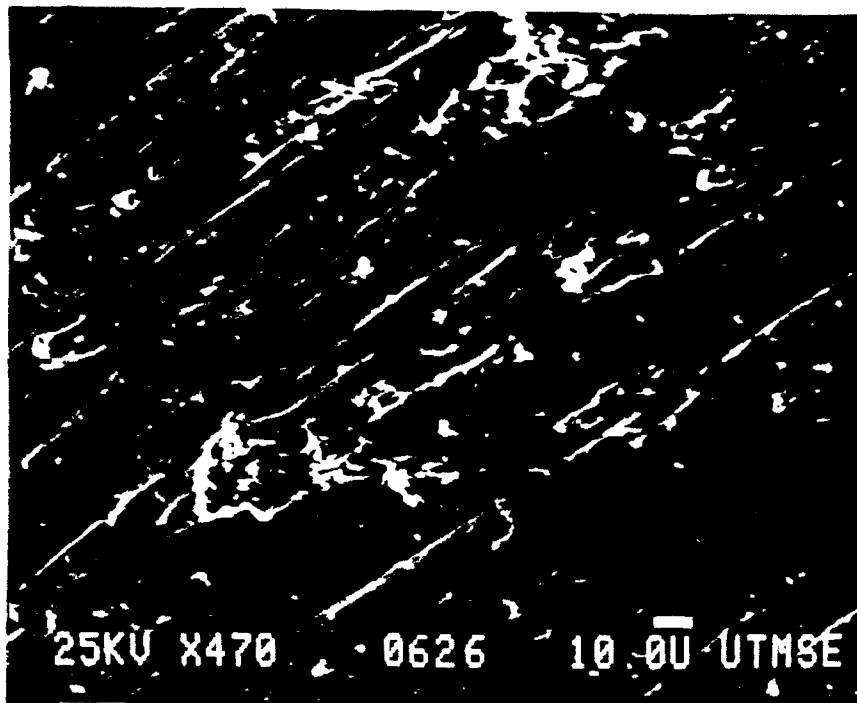
Figure 5a. SEM micrograph of an as-polished 25 vol % Gr$_p$ Cu MMC.

Figure 5b. SEM micrograph of a polished and etched 25 vol % Gr$_p$ Cu MMC.

Figure 6. SEM micrograph of an as-polished 50 vol % Gr$_f$/C MMC demonstrating the alignment and distribution of the reinforcement.
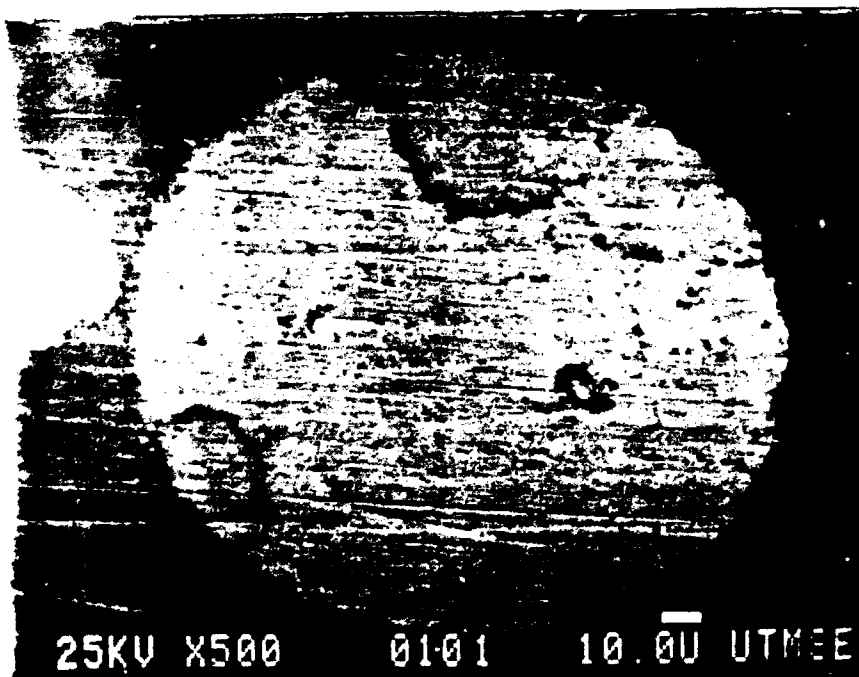
Figure 7. SEM micrograph of an as-polished 70 % W$_f$/Cu MMC.
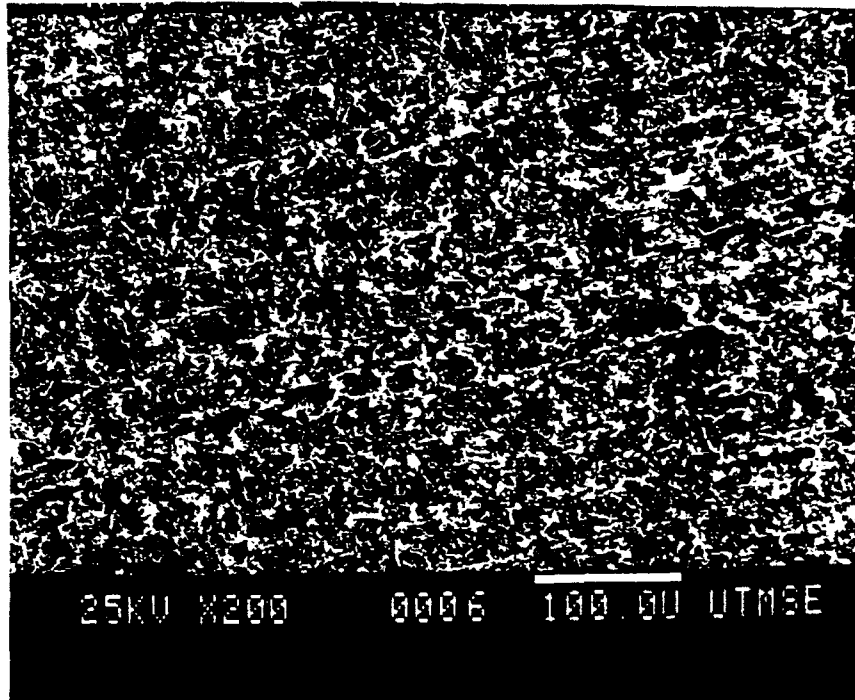
Figure 8a. SEM micrograph of ETP Copper after 6 hours immersion in aerated 3.5 wt % NaCl.

Figure 8b. SEM micrograph of ETP Copper after 6 hours immersion in deaerated 3.5 wt % NaCl.
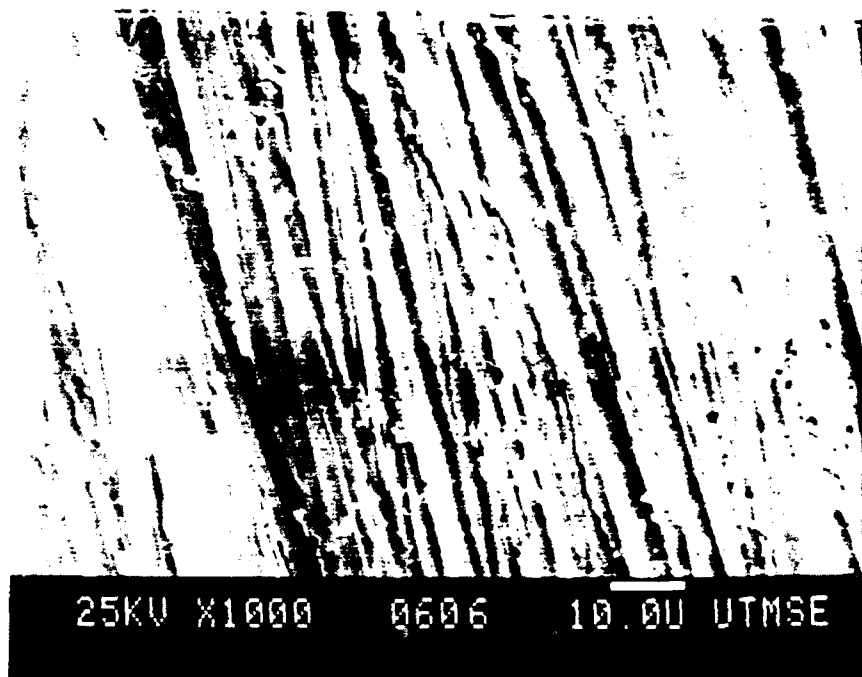
Figure 9a. SEM micrograph of HEHR 100% Copper after 6 hours immersion in aerated 3.5 wt %
NaCl.
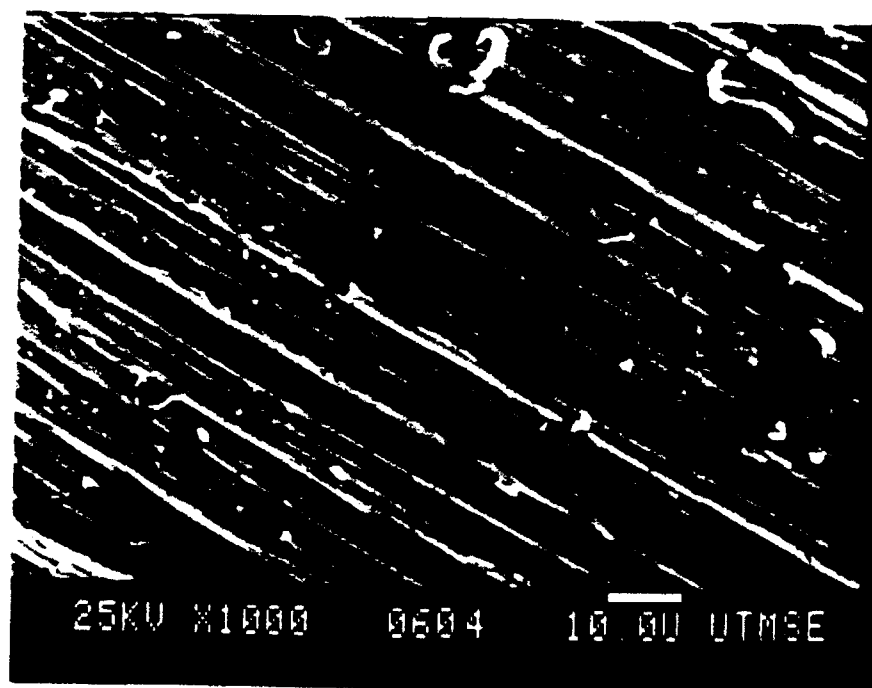
Figure 9b. SEM micrograph of HEHR 100 % Copper after 6 hours immersion in deaerated 3.5
wt % NaCl.
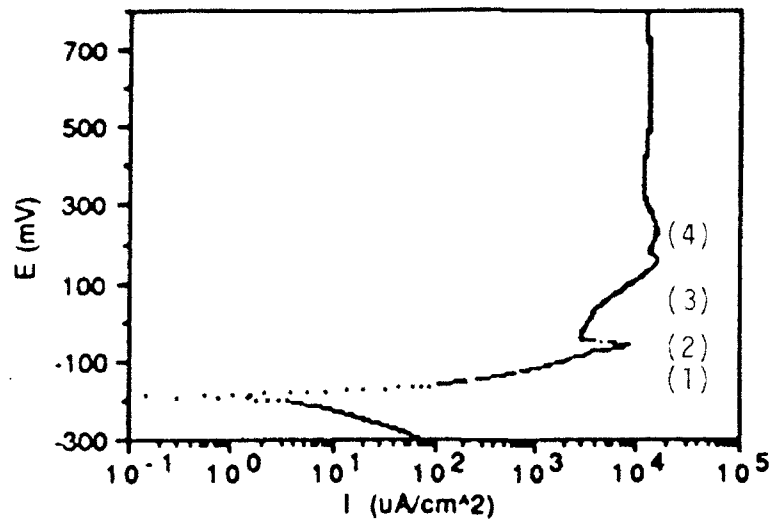
Figure 10a. Typical polarization curve for ETP Copper in aerated 3.5 wt % NaCl.
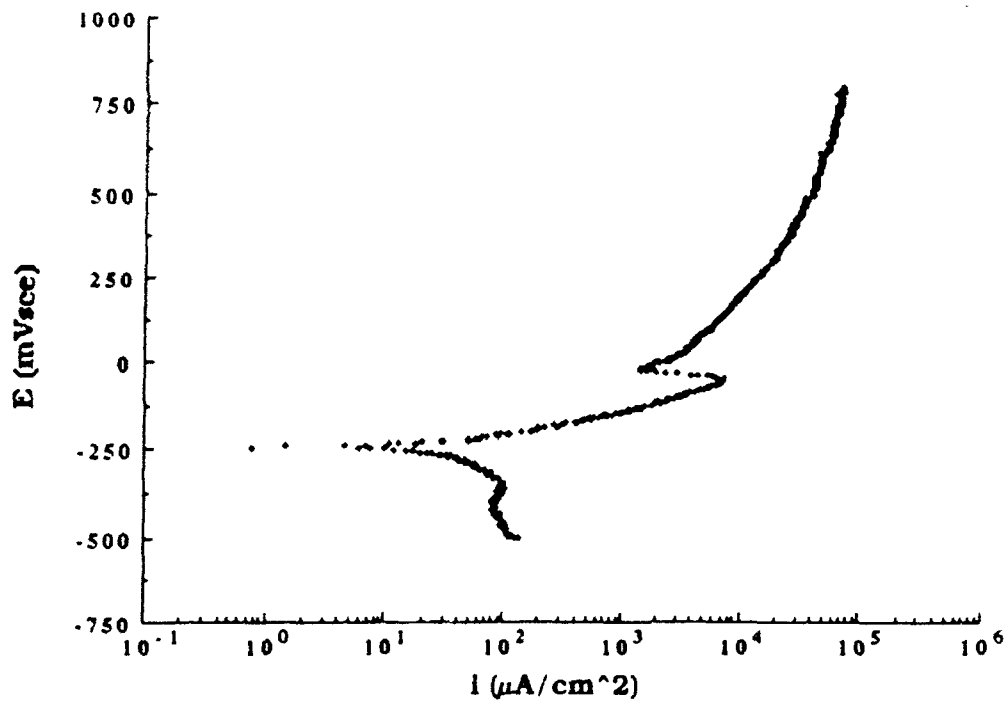(Scan rate = 1 mV/sec)
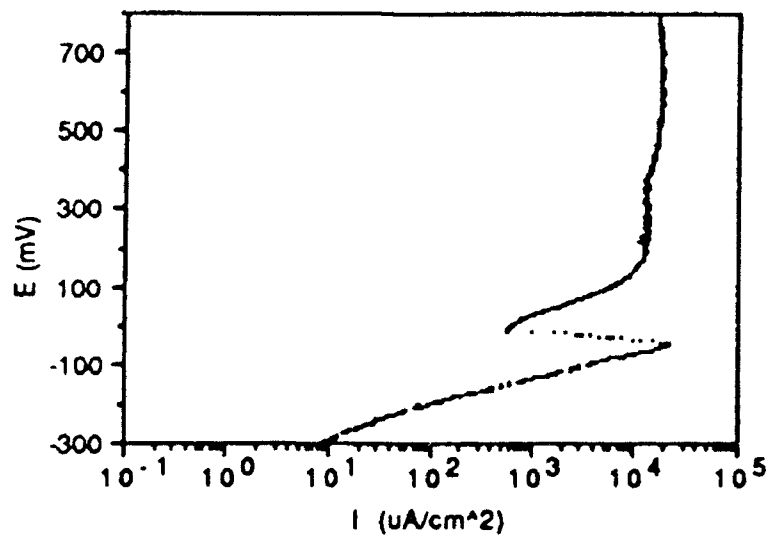
Figure 10b. Typical polarization curve for ETP Copper in deaerated 3.5 wt % NaCl.
(Scan rate = 1 mV/sec)
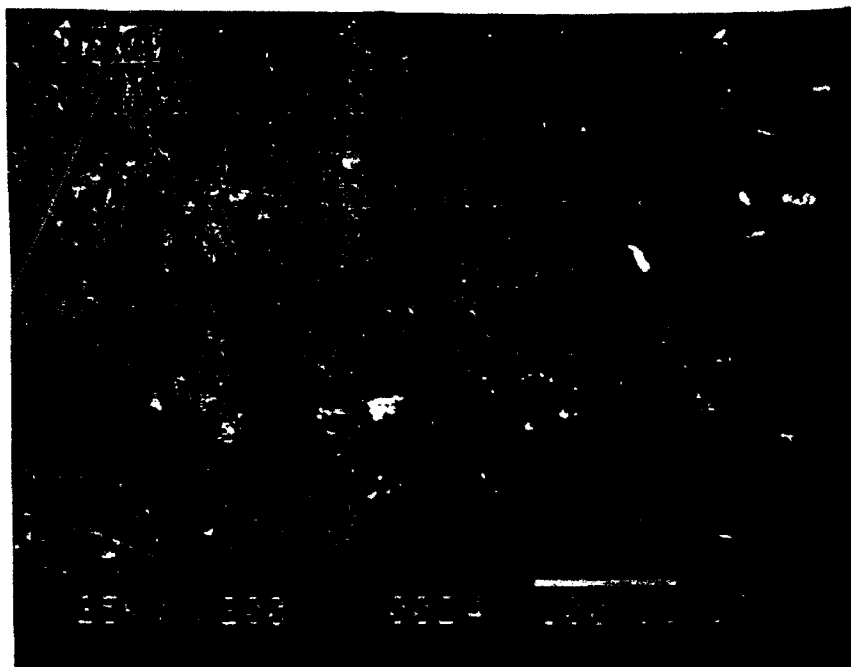
Figure 11a. SEM micrograph of DS Copper after 6 hours immersion in aerated 3.5 w% NaCl.
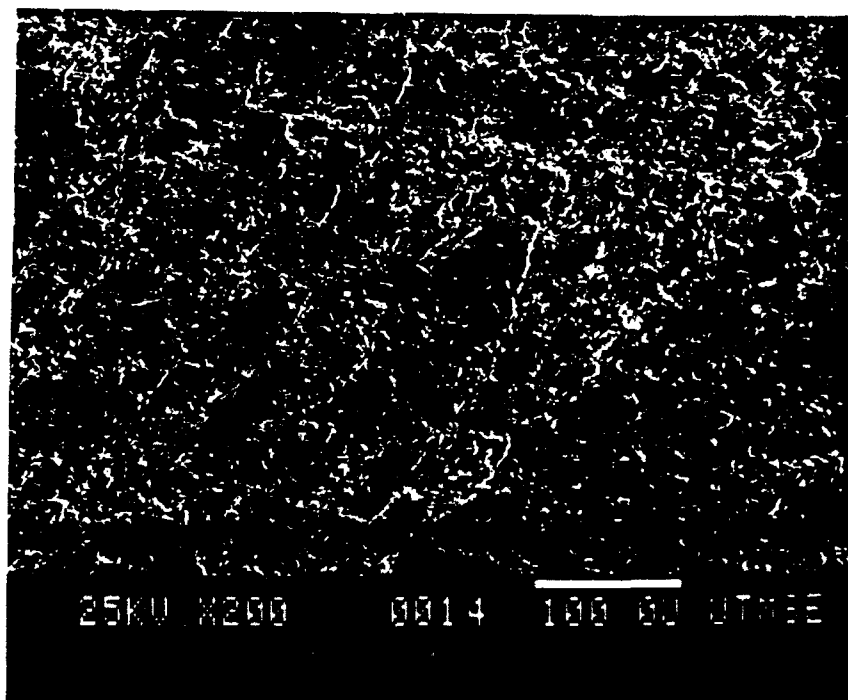
Figure 11b. SEM micrograph of DS Copper after 6 hours immersion in deaerated 3.5 w% NaCl.
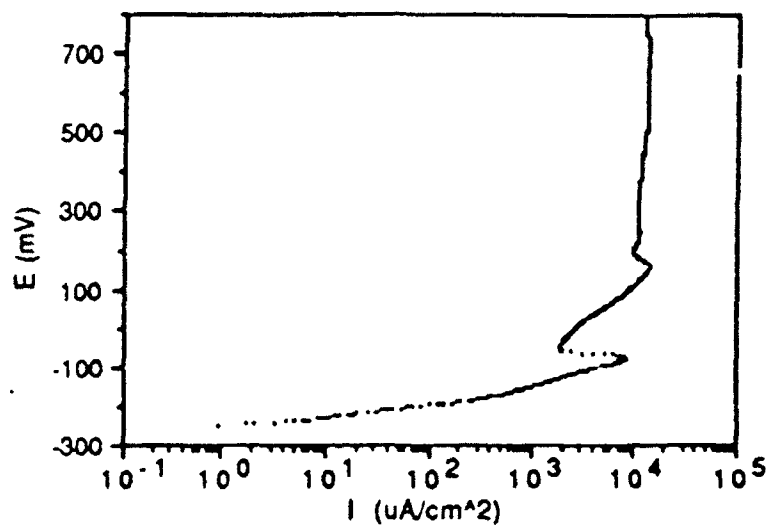
Figure 12a. Typical anodic polarization curve for DS Copper in aerated 3.5 wt % NaCl. (Scan rate = 1 mV/sec)
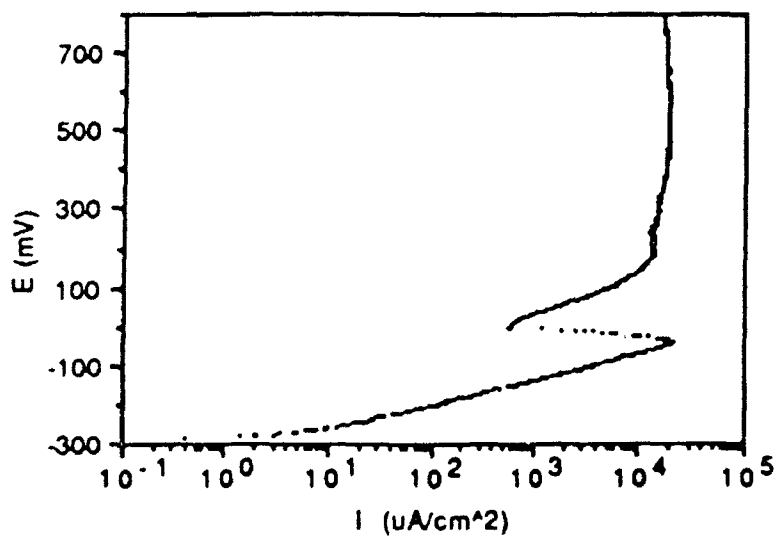
Figure 12b. Typical anodic polarization curve for DS Copper in deaerated 3.5 wt % NaCl. (Scan rate = 1 mV/sec)
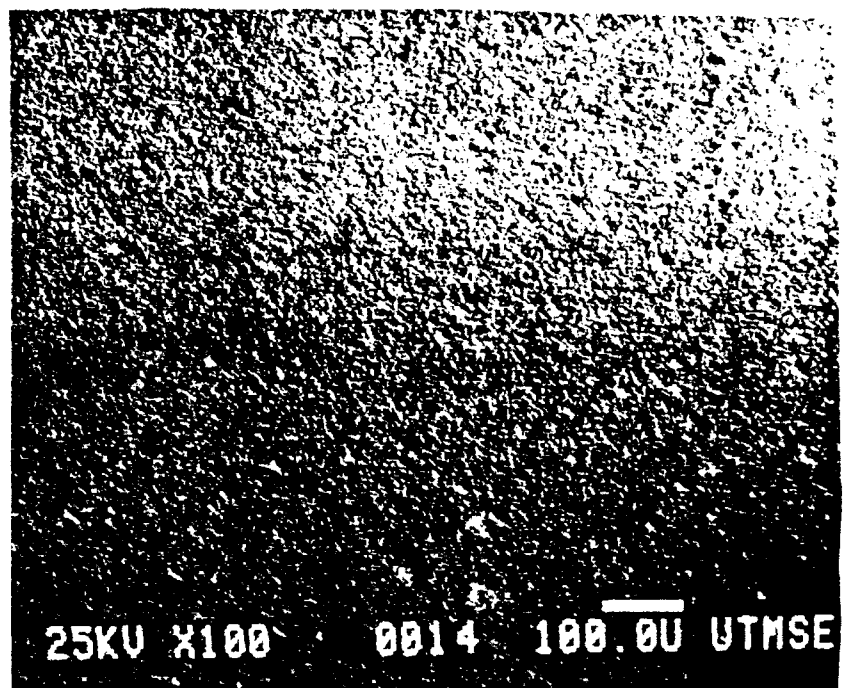
Figure 13a. SEM micrograph of ETP Copper after anodic polarization in aerated 3.5 wt % NaCl.

Figure 13b. SEM micrograph of DS Copper after anodic polarization in aerated 3.5 wt % NaCl.
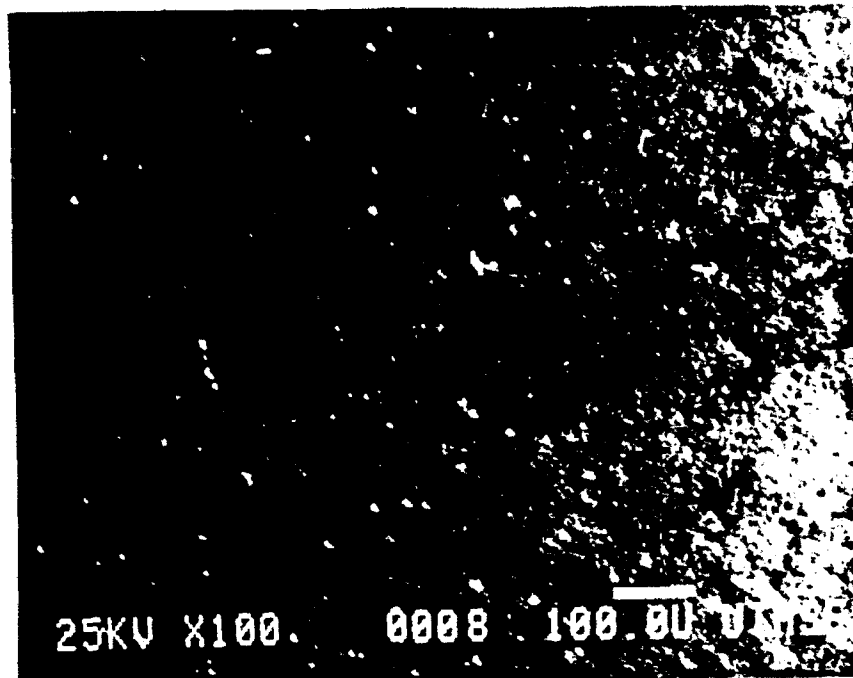
Figure 14a. SEM micrograph of ETP Copper after anodic polarization in deaerated 3.5 wt % NaCl.
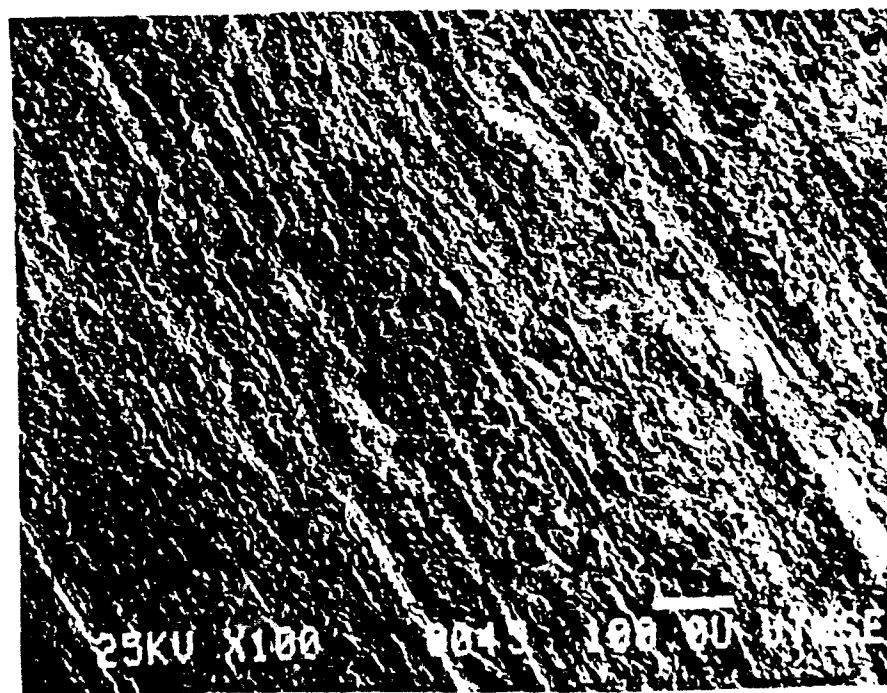
Figure 14b. SEM micrograph of DS Copper after anodic polarization in deaerated 3.5 wt % NaCl
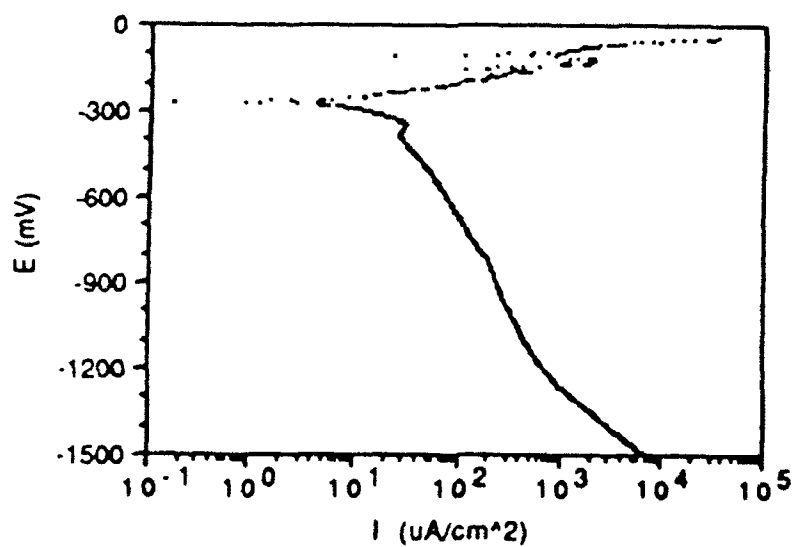
Figure 15a. Typical cathodic polarization curve for ETP Copper in deaerated 3.5 wt % NaCl.
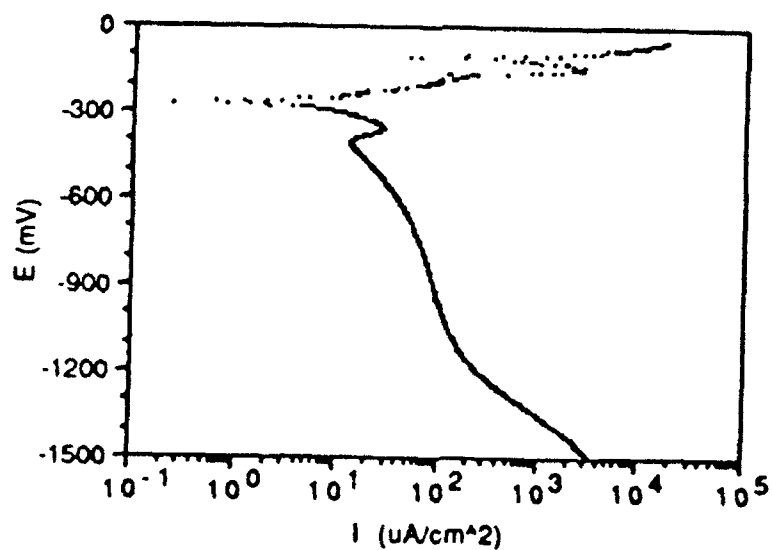
Figure 15b. Typical cathodic polarization curve for DS Copper in deaerated 3.5 wt % NaCl.

(a)

(b)

25KV X200 0006 100.0U UTMSE

(c)

25KU X200 0003 100.0U UTMSE
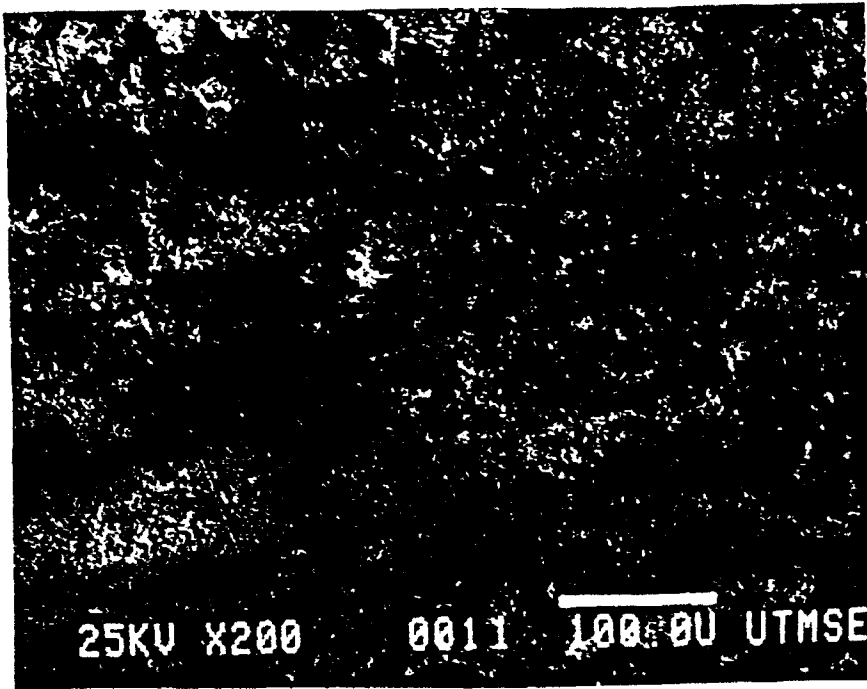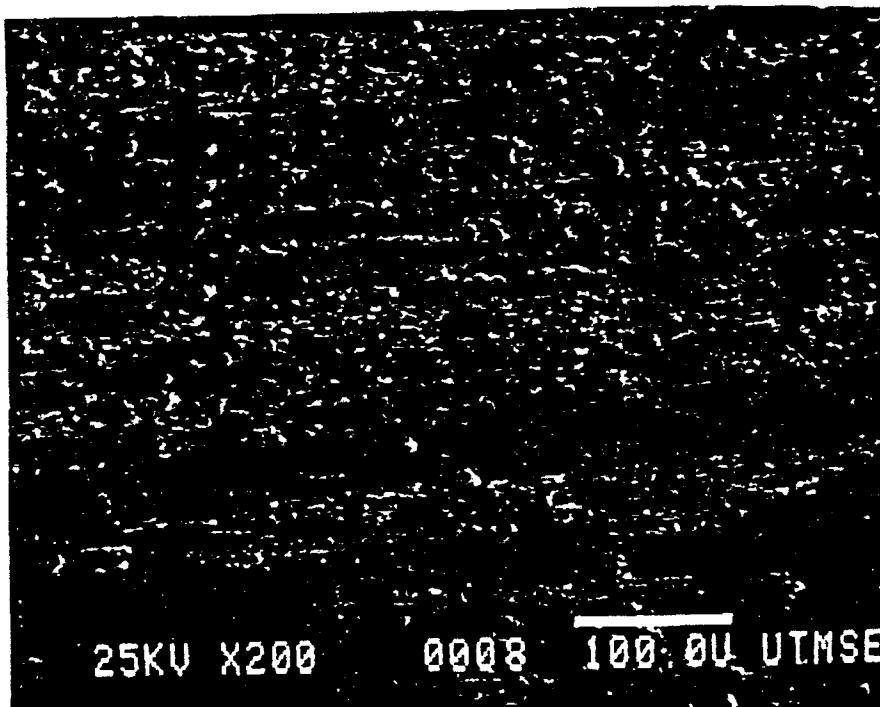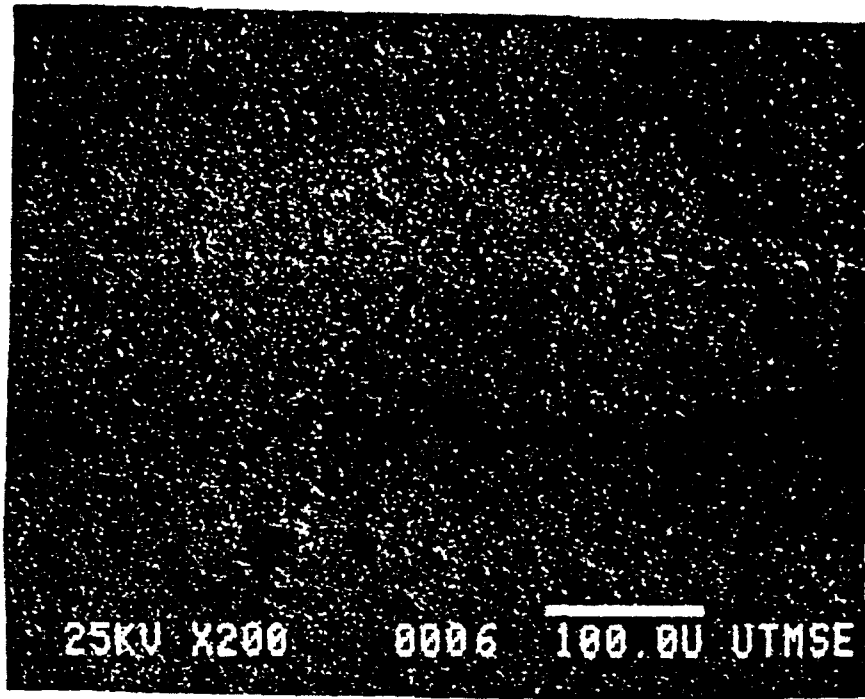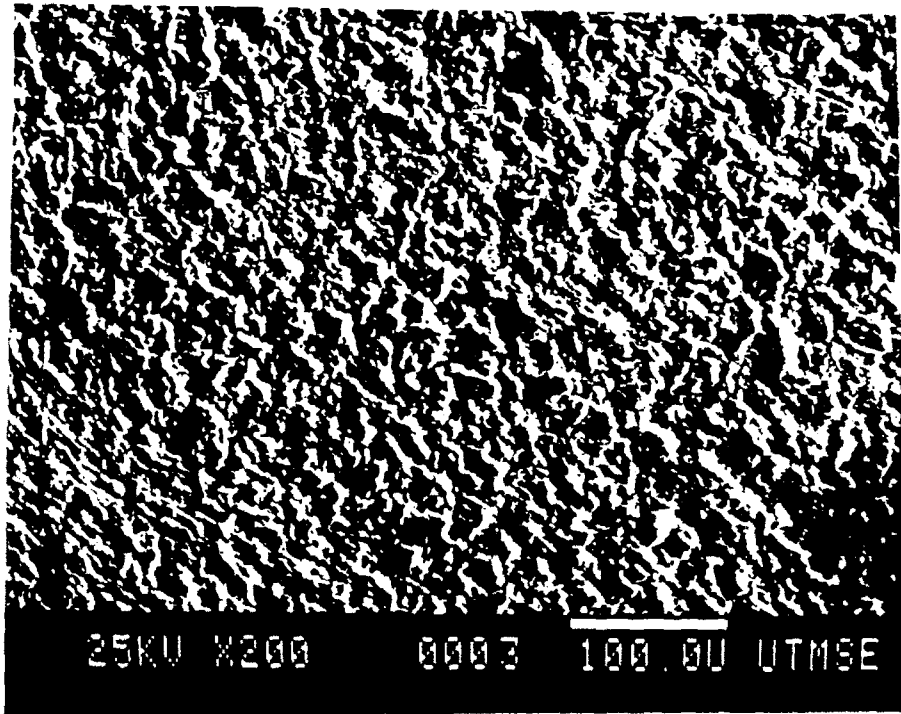
(d)
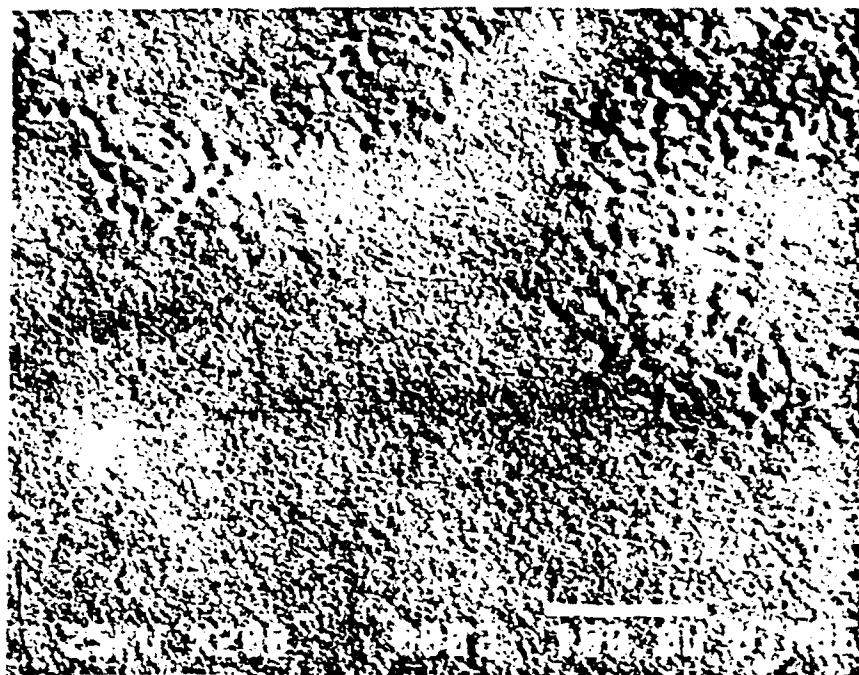
(e)

Figure 16a. SEM micrographs of DS Copper after potentiostatic polarization at applied potentials of (a) -200 mV vs SCE (b) -80 mV vs SCE (c) 0 mV vs SCE (d) 200 mV vs SCE (e) 600 mV vs SCE.

Bakelite

stainless steel

Teflon

sample

stainless steel spring
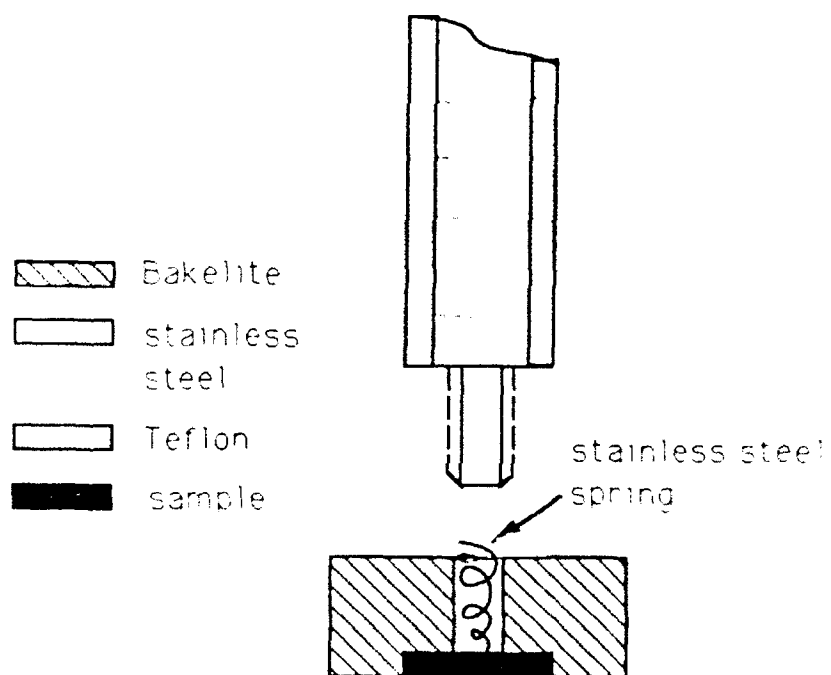
Figure 17a. Schematic representation of the rotating disk electrode assembly.
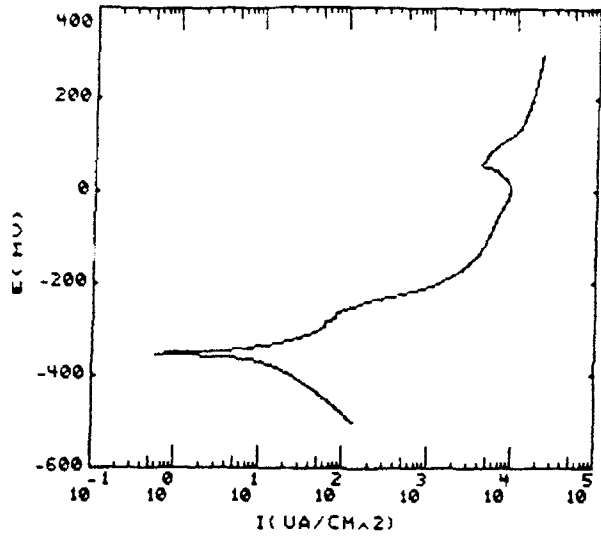
(b)
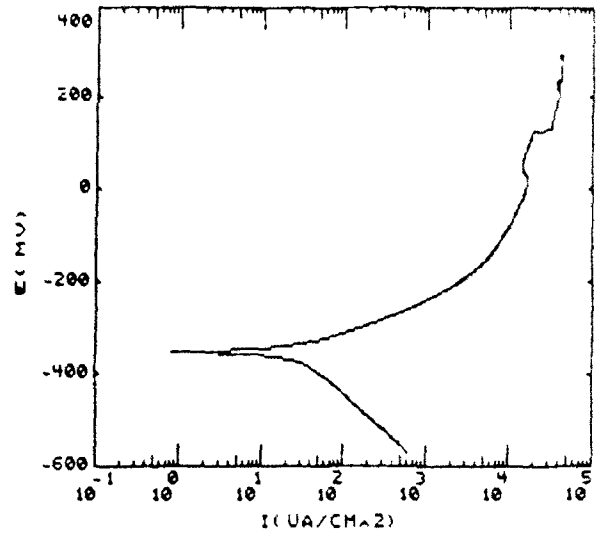
(c)
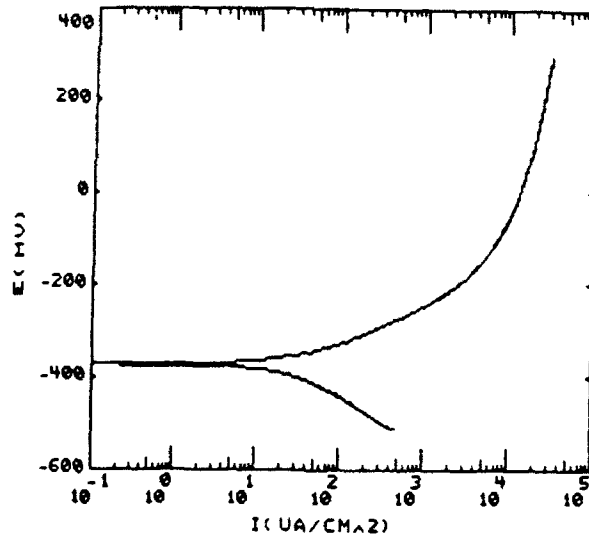
(d)

Figure 17b. Typical anodic polarization curve for DS Cu in open to air 3.5 wt % NaCl at 1000 rpm

Figure 17c. Typical anodic polarization curve for DS Cu in open to air 3.5 wt % NaCl at 3000 rpm.

Figure 17d. Typical anodic polarizaton curve for DS Cu in open to air 3.5 wt % NaCl at 5000 rpm.
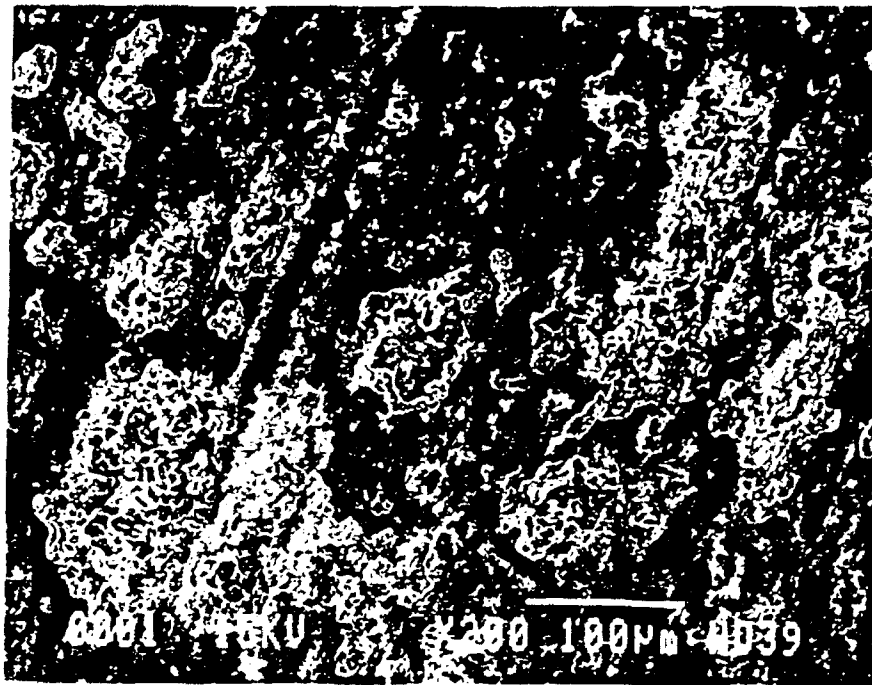
Figure 18. SEM micrograph of the most highly stressed region of a U-bend specimen made from DS Copper and exposed to 3.5 wt % NaCl for 4 months. The sample was cleaned in 1 wt % H_2SO_4 and then rinsed in distilled water.

Figure 19. SEM micrograph of the most highly stressed region of an exposed U-bend specimen made from DS Copper and exposed to 3.5 wt % artificial seawater for 4 months. The specimen was not cleaned prior to taking the micrograph.
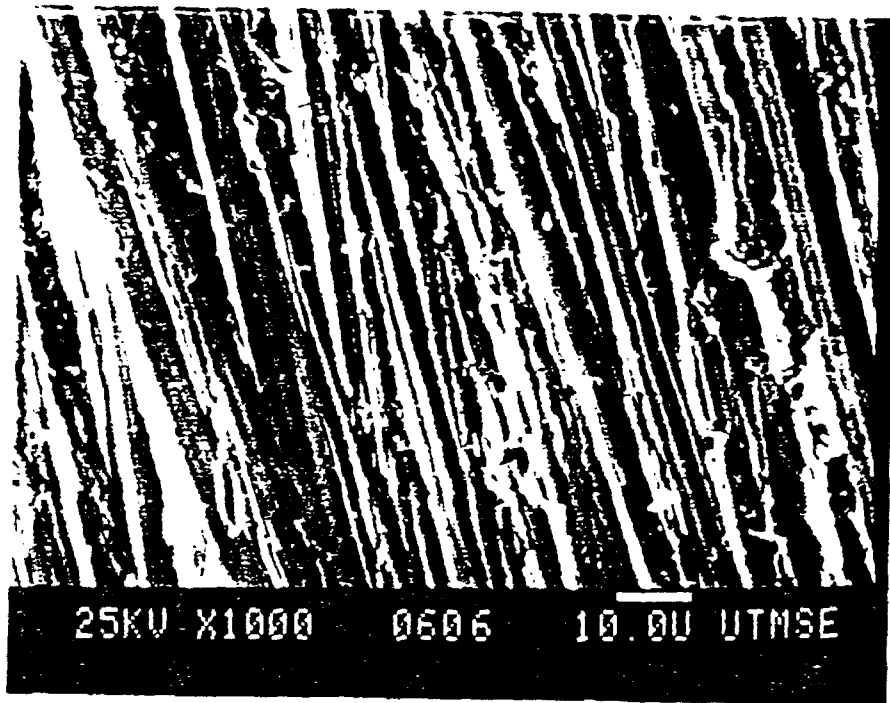
Figure 20a. SEM micrograph of HEHR 100% Copper after 4 hours immersion in aerated 3.5 wt % NaCl.
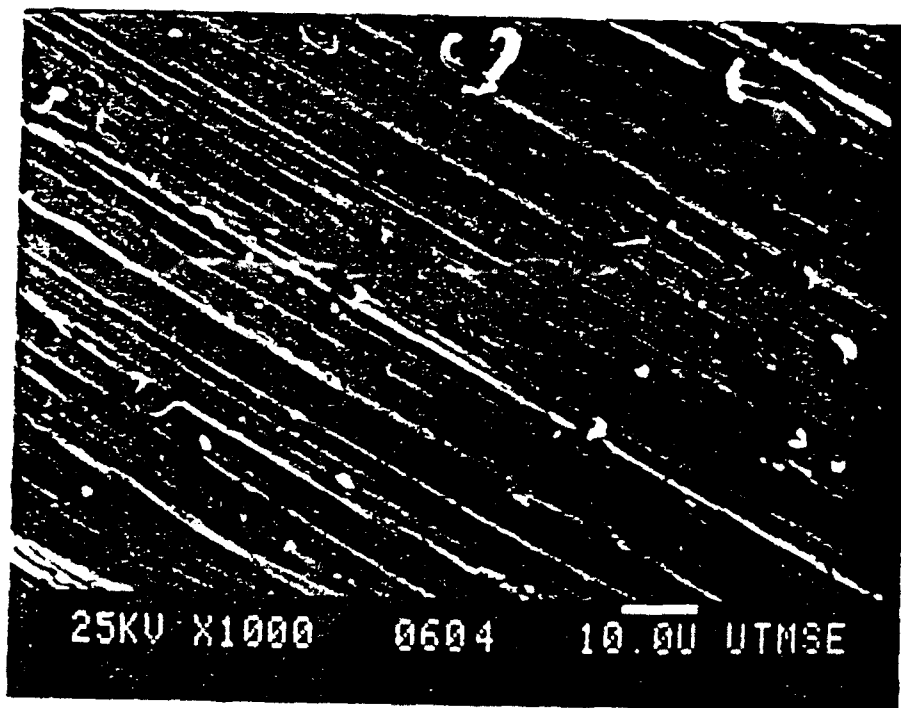
Figure 20b. SEM micrograph of HEHR 100% Copper after 4 hours immersion in deaerated 3.5 wt % NaCl.
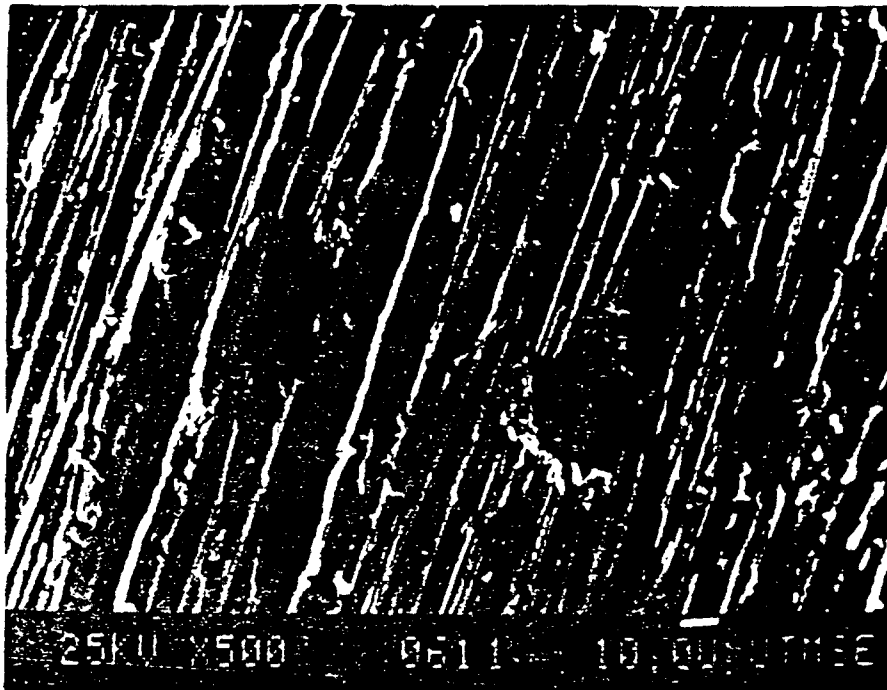
Figure 20c. SEM micrograph of a 15 vol % Gr$_p$/Cu MMC after 4 hours immersion in aerated 3.5 wt % NaCl.
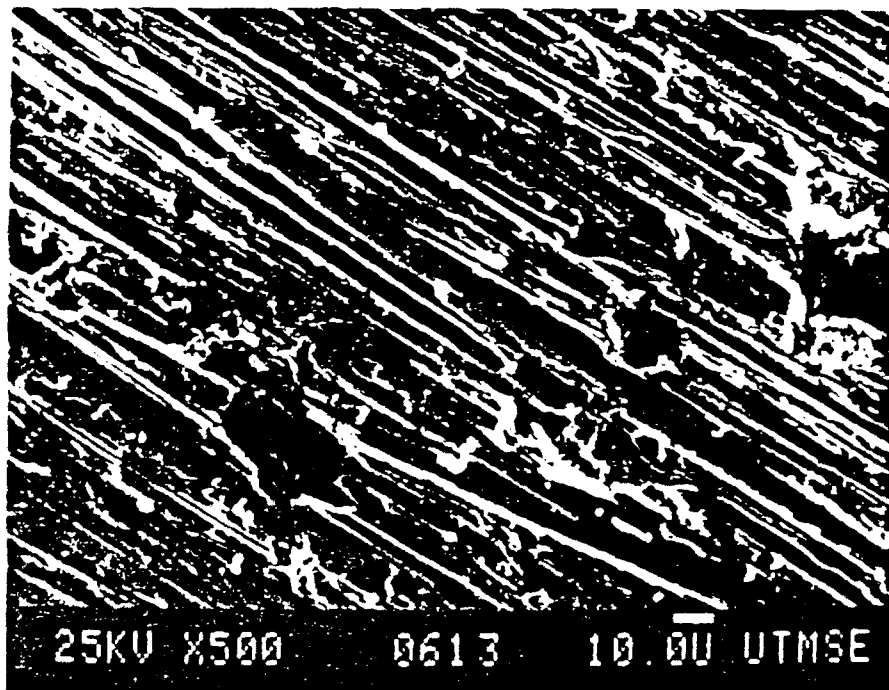
Figure 20d. SEM micrograph of a 15 vol % Gr$_p$/Cu MMC after 4 hours immersion in deaerated 3.5 wt % NaCl.
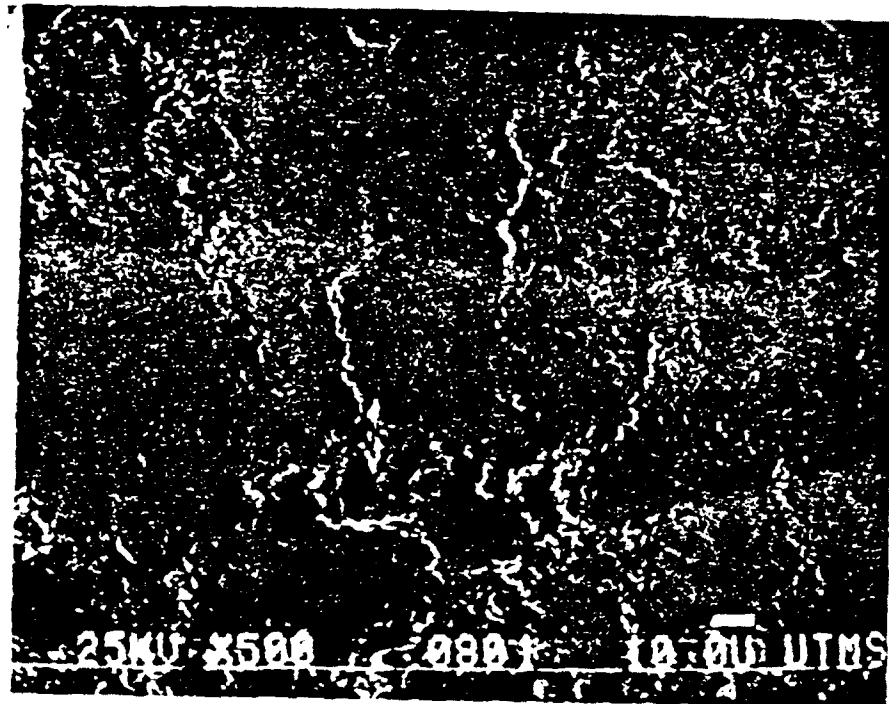
Figure 20e. SEM micrograph of a 40 vol % Gr$_p$/Cu MMC after 4 hours immersion in aerated 3.5 wt % NaCl.
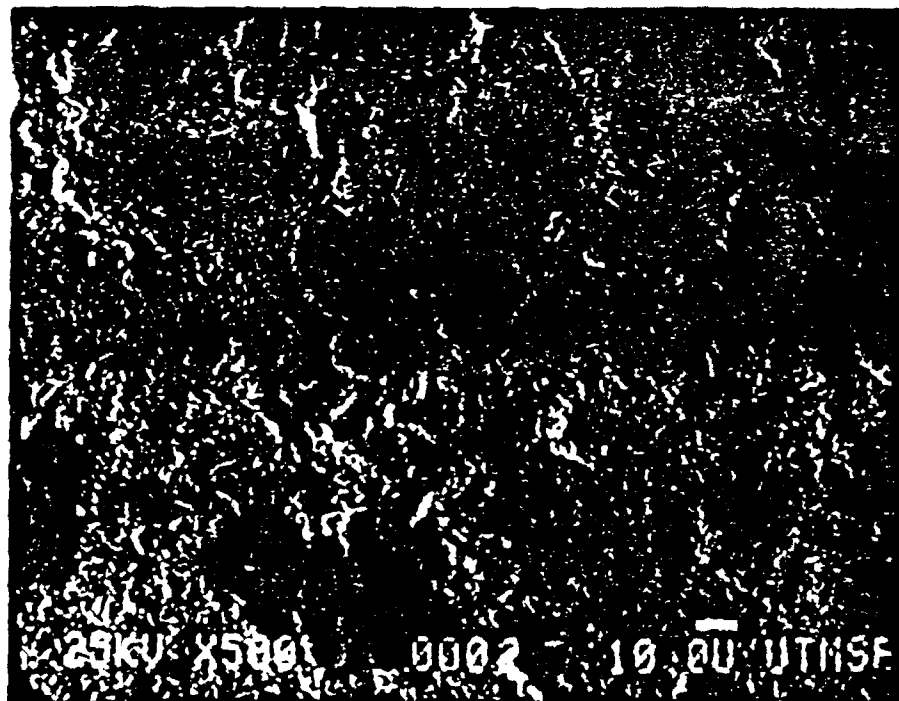
Figure 20f. SEM micrograph of a 40 vol % Gr$_p$/Cu MMC after 4 hours immersion in deaerated 3.5 wt % NaCl.

Figure 21. SEM micrograph of a 1.2 vol % Gr_p/Cu MMC after 10 hours immersion in aerated 3.5 wt % NaCl.
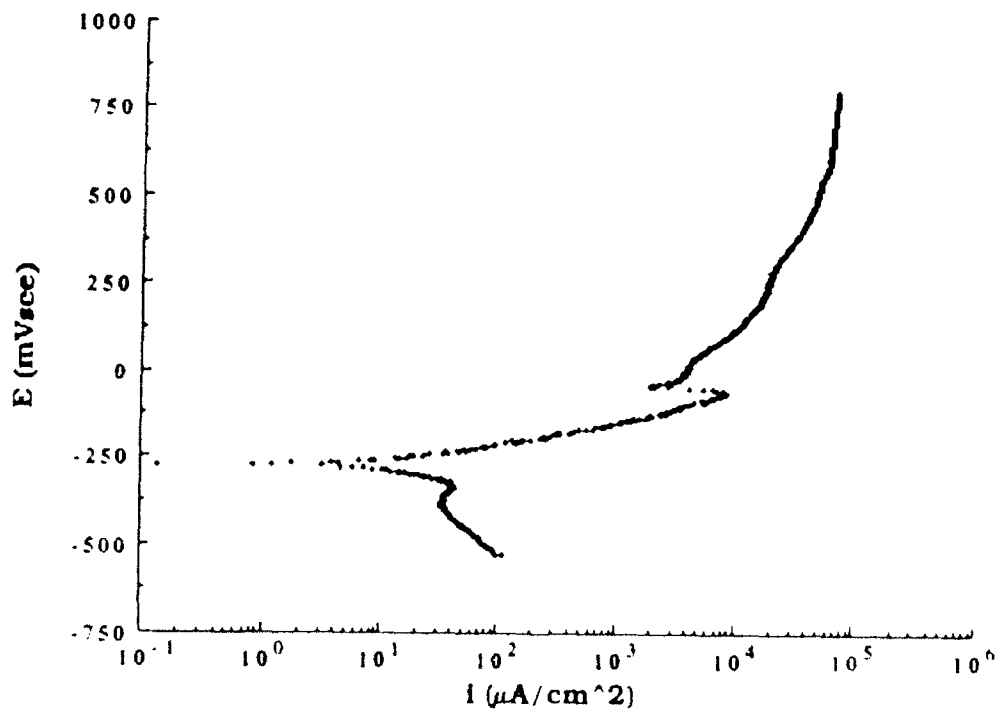
Figure 22a. Typical polarization curve for ETP Copper in aerated 3.5 wt % NaCl. (Scan rate was 0.2 mV/sec)

Figure 22b. Typical polarization curve for a 5 vol % Gr$_p$/Cu MMC in aerated 3.5 wt % NaCl. (Scan rate was 0.2 mV/sec)
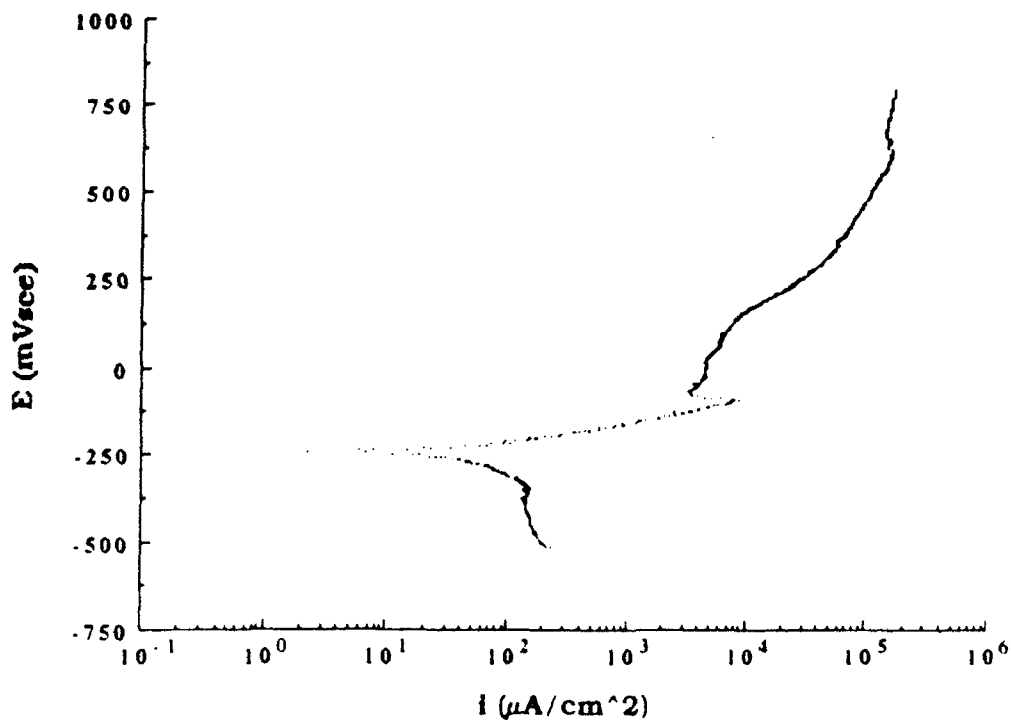
Figure 22c. Typical polarization curve for a 15 vol % Gr$_p$/Cu MMC in aerated 3.5 wt % NaCl. (Scan rate was 0.2 mV/sec)
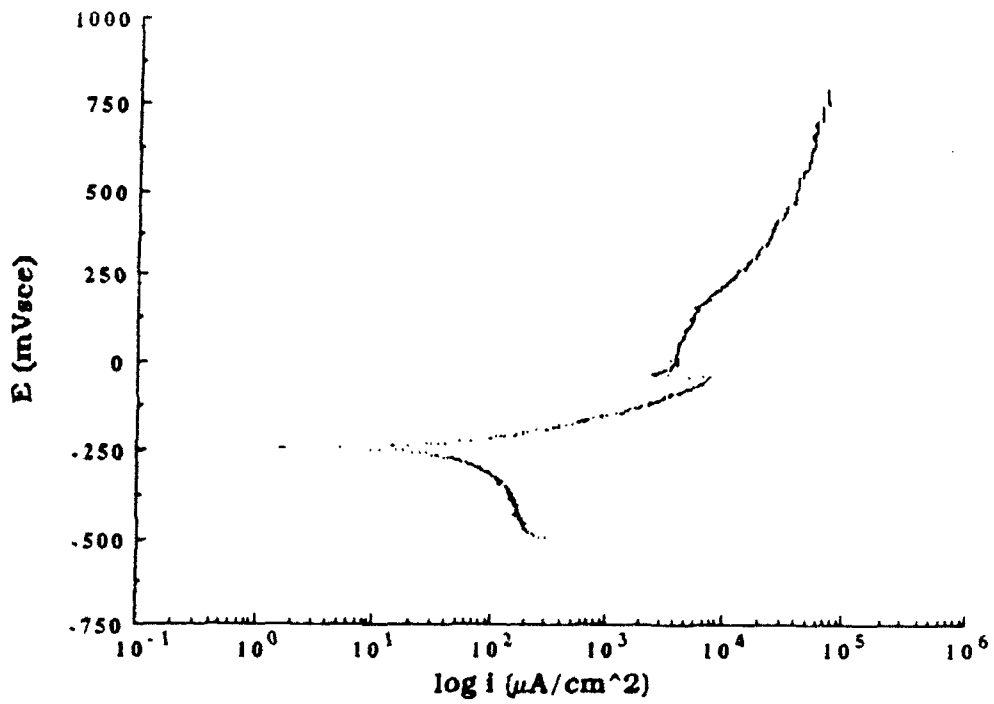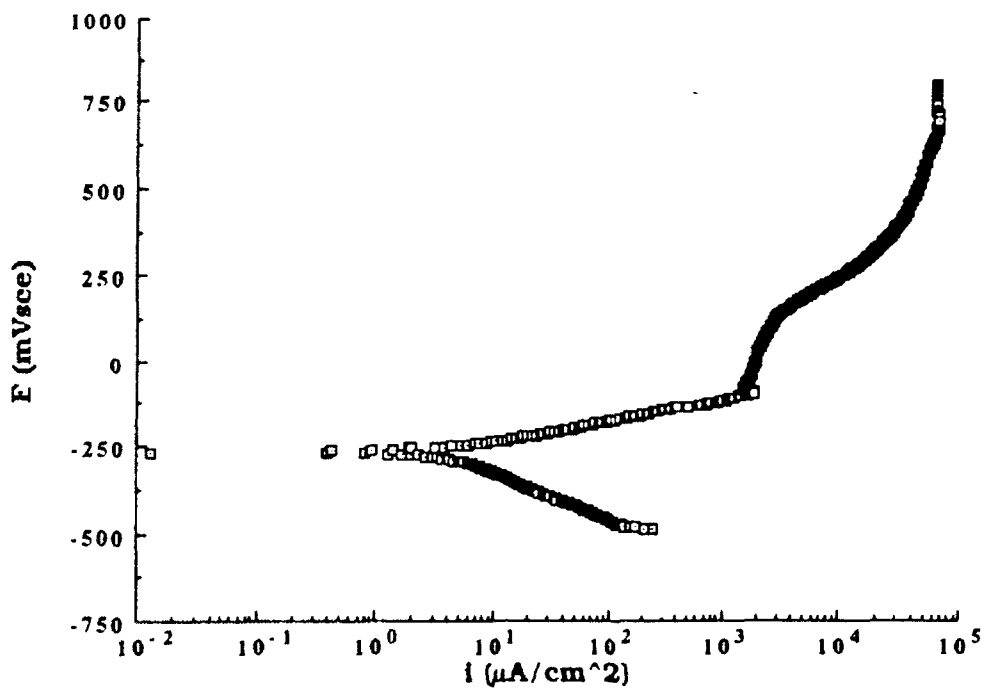
Figure 23a. Typical polarization curve for a 25 vol % Gr_p/Cu MMC in aerated 3.5 wt % NaCl. (Scan rate was 0.2 mV/sec)
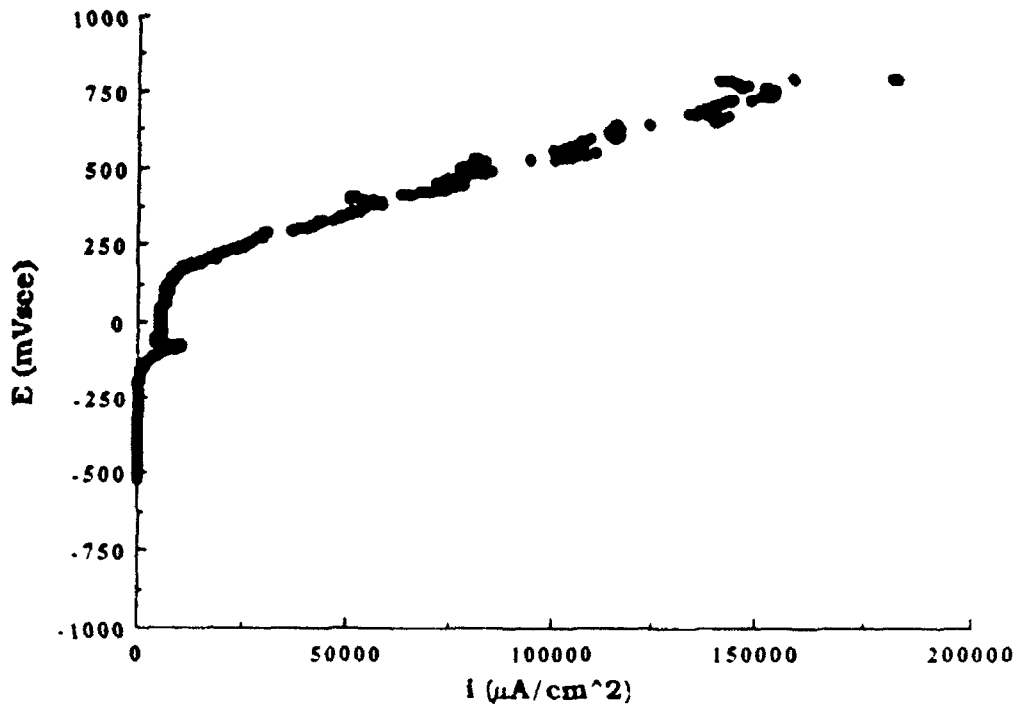

Figure 23b. Another plot of the data in Figure 23a in which the graph emphasizes the jumps in anodic current density due to exfoliation of the composite.
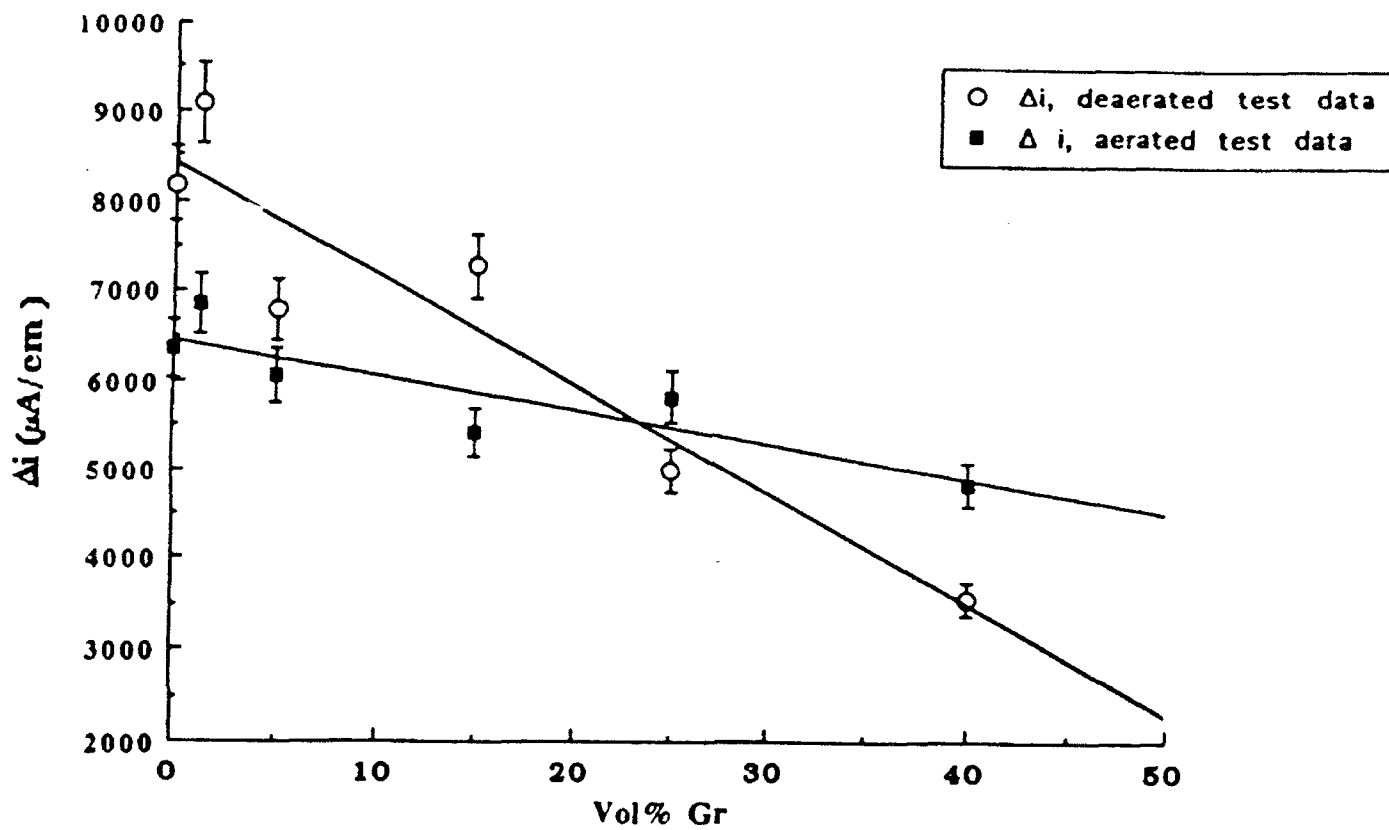
Figure 24. Difference between maximum and minimum current density in region 2 as a function of vol % graphite.
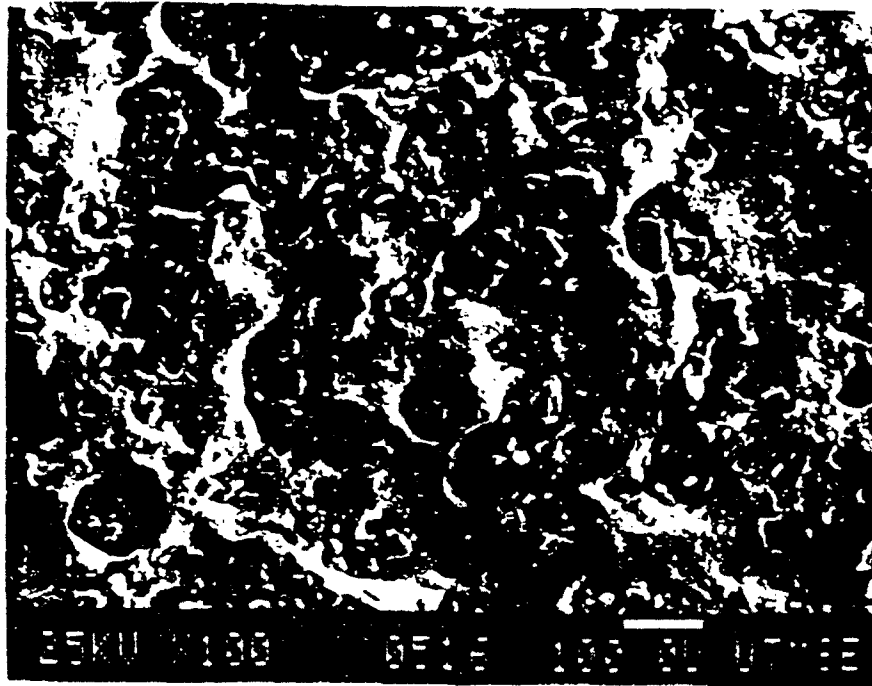
Figure 25a. SEM micrograph of a 5 vol % Gr$_p$/Cu MMC after anodic polarization in deaerated 3.5 wt % NaCl.
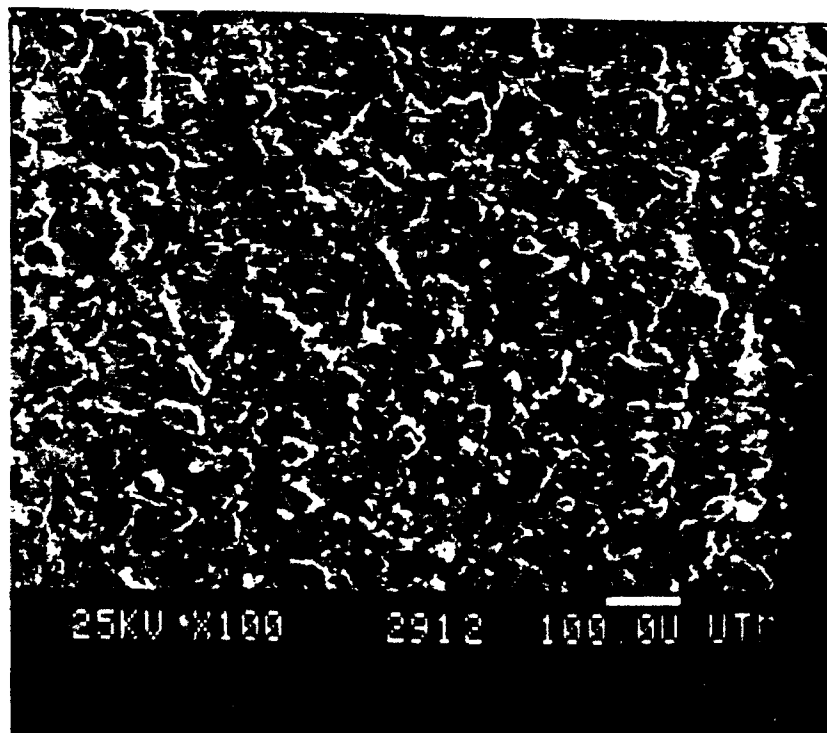
Figure 25b. SEM micrograph of a 25 vol % Gr$_p$/Cu MMC after anodic polarization in deaerated 3.5 wt % NaCl.
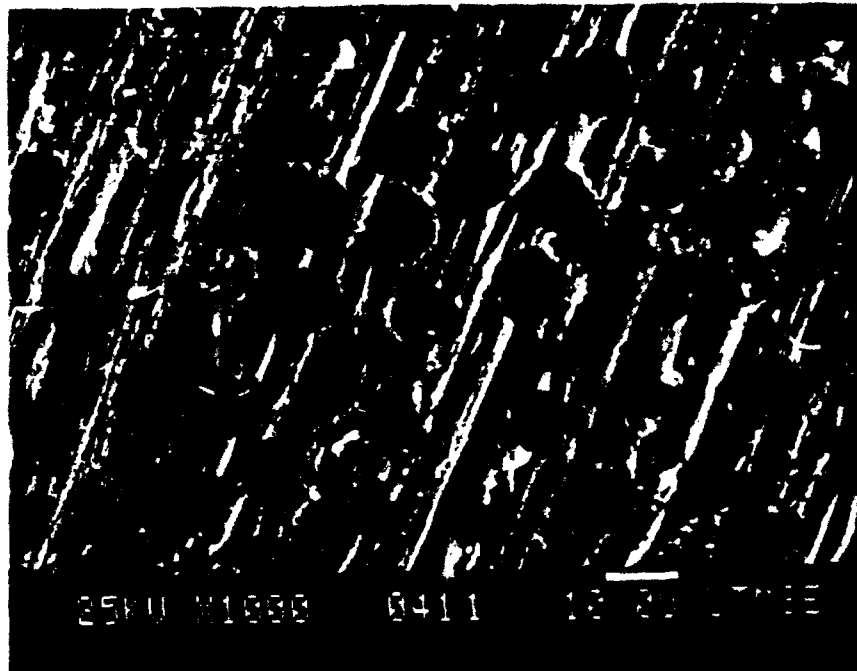
Figure 26. SEM micrograph of a 50 vol % Grf/Cu MMC after 5 hours immersion in deaerated 3.5 wt % NaCl..
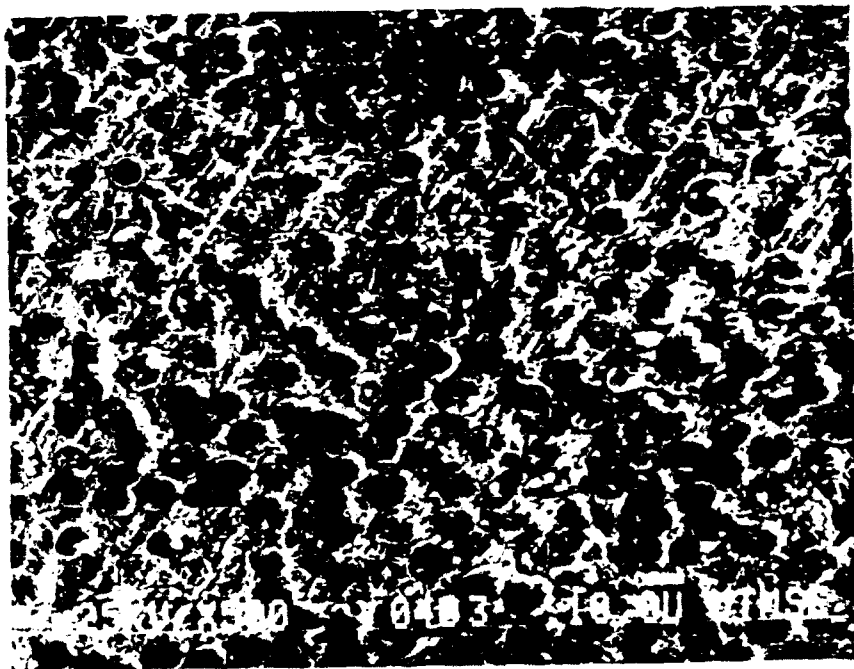
Figure 27a. SEM micrograph of a 50 vol % Grf/Cu MMC after an anodic Tafel test in deaerated 3.5 wt % NaCl.
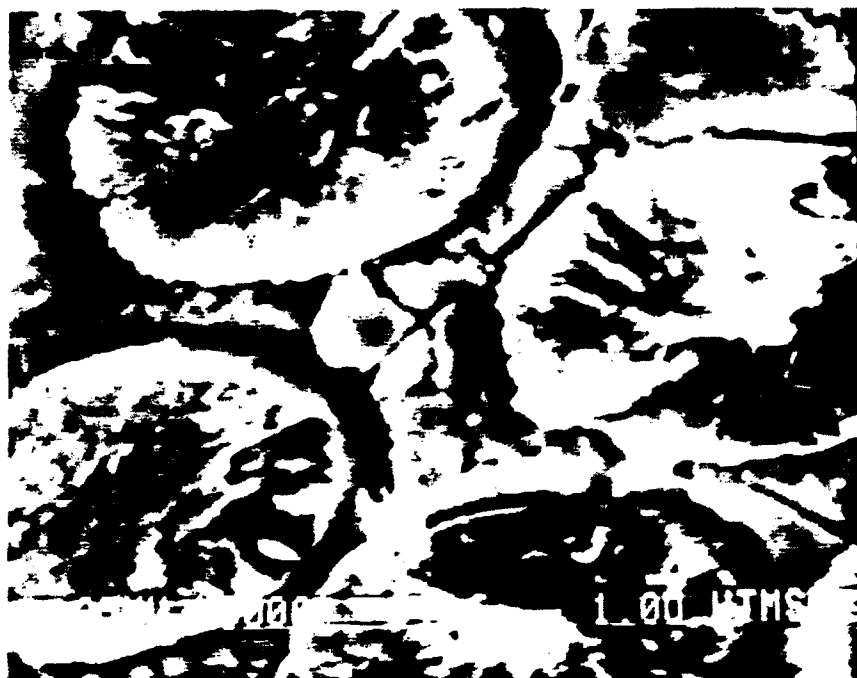
Figure 27b. A higher magnification of the composite in Figure 27a.
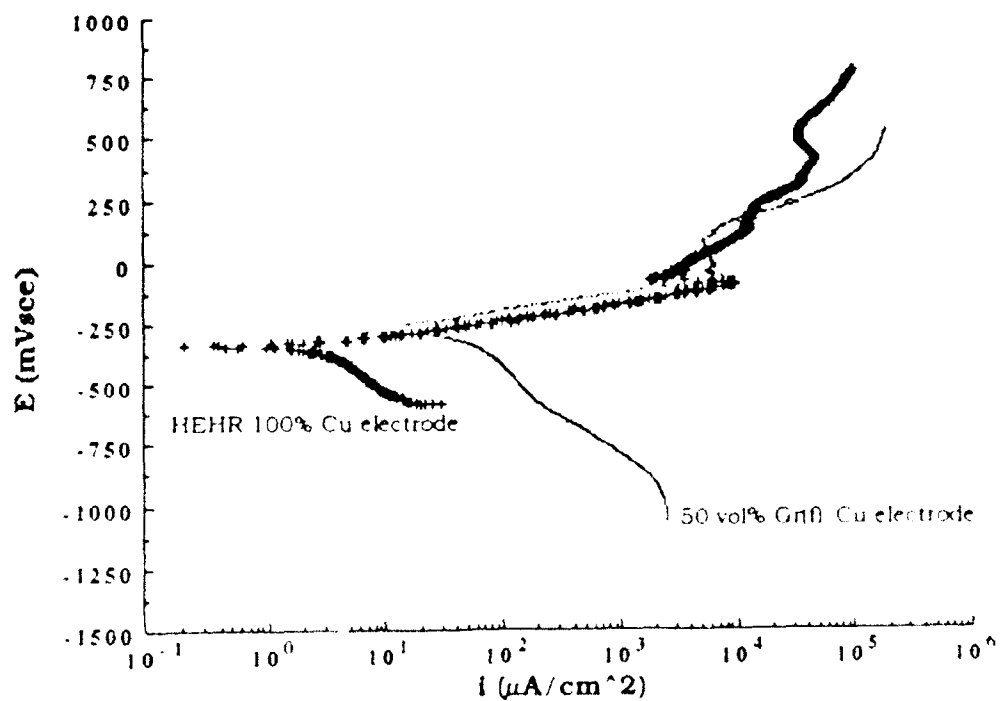
Figure 28. Typical polarization curves for HEHR 100% Copper and a 50 vol % Gr$_f$ Cu MMC in deaerated 3.5 wt % NaCl. (Scan rates were 0.2 mV/sec.)
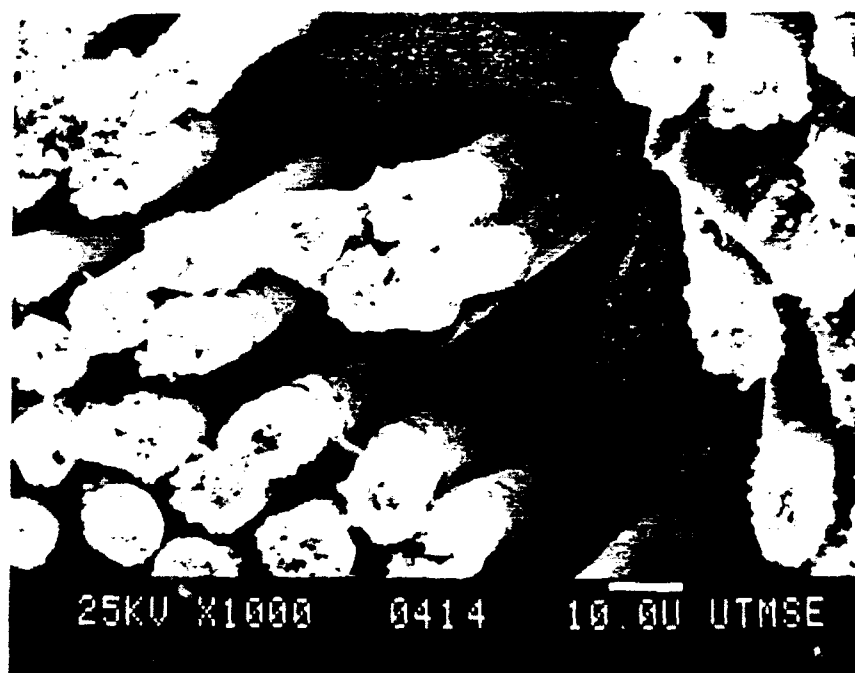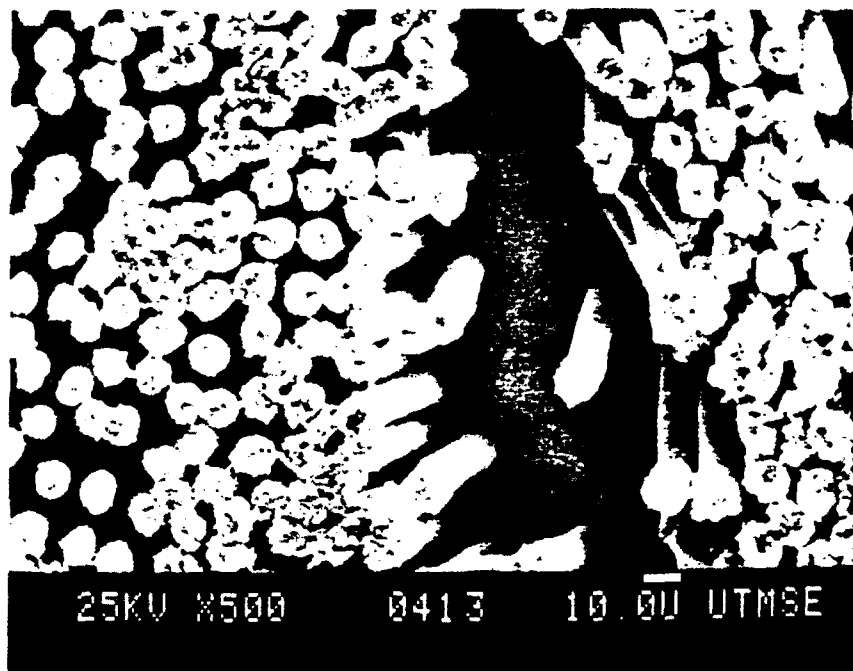
Figure 29a. SEM micrograph of a 50 vol % Grf/Cu MMC after anodic polarization to 800 mV vs SCE in deaerated 3.5 w% NaCl.

Figure 29b. Higher magnification of the composite in Figure 29a.
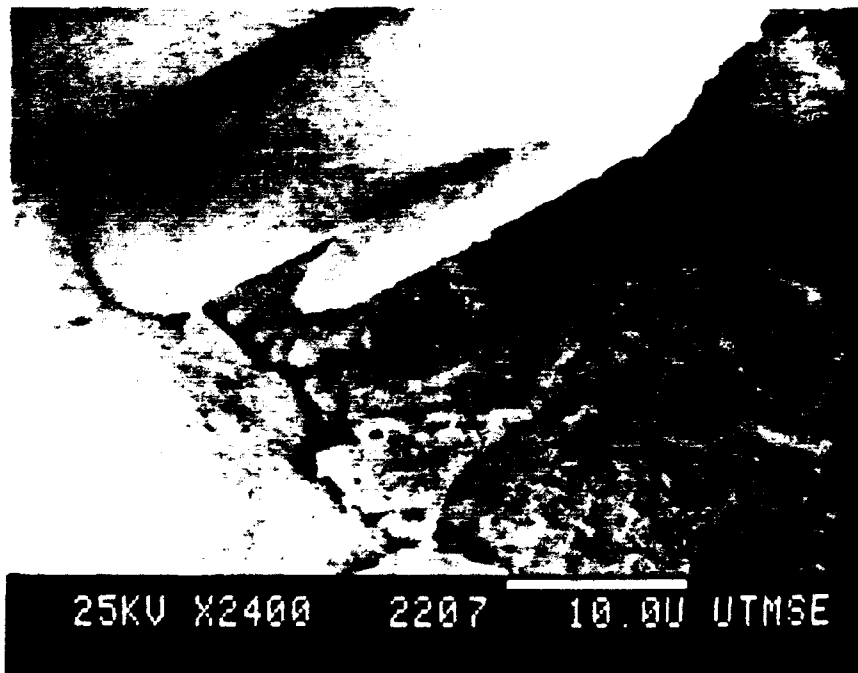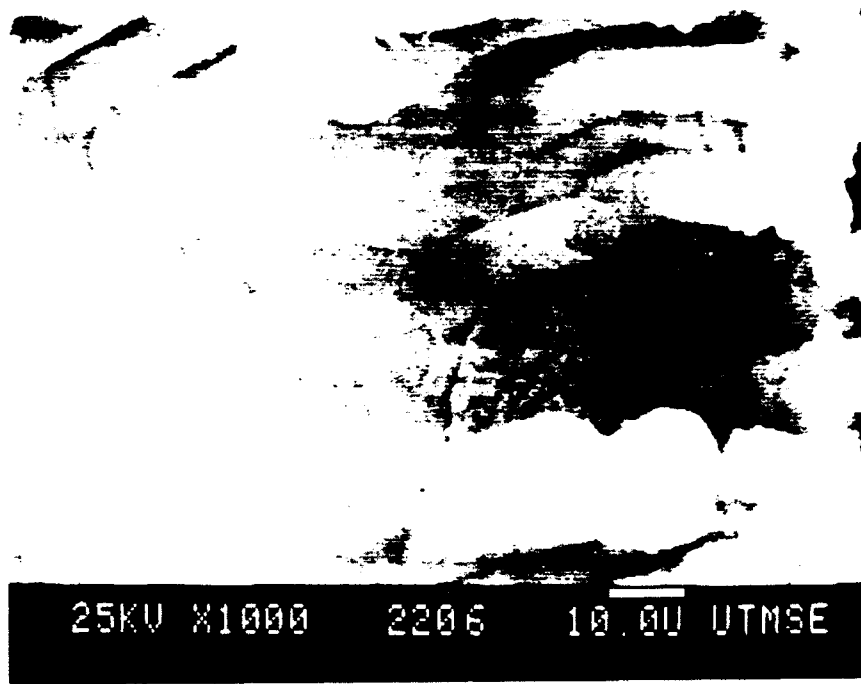
Figure 30a. SEM micrograph of a 50 v% Gr$_f$ Cu MMC after anodic polarization to 800 mV vs
SCE in aerated 3.5 w% NaCl.

Figure 30b. Higher magnification of the composite in Figure 30a.
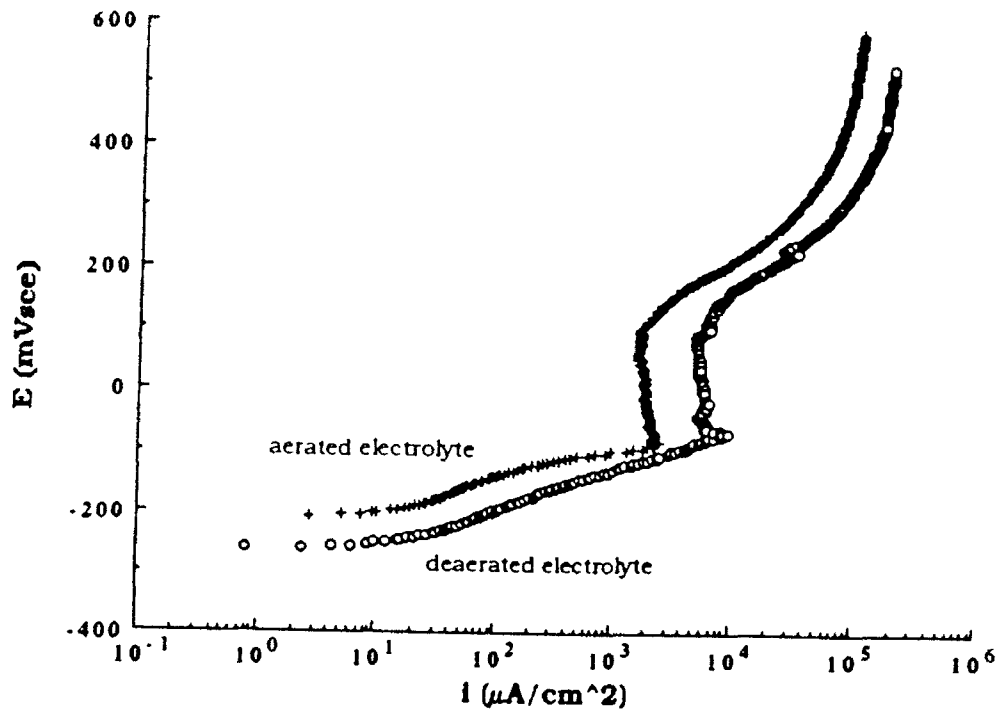
Figure 31. Typical anodic polarization curves for 50 vol %Gr$_f$/Cu MMCs in aerated and deaerated - 3.5 wt % NaCl. (Scan rates were 0.2 mV/sec)

Figure 32. Typical anodic polarization curve for a 70 vol % W$_f$/Cu MMC in aerated 3.5 wt % NaCl.(Scan rate was 0.2 mV/sec)
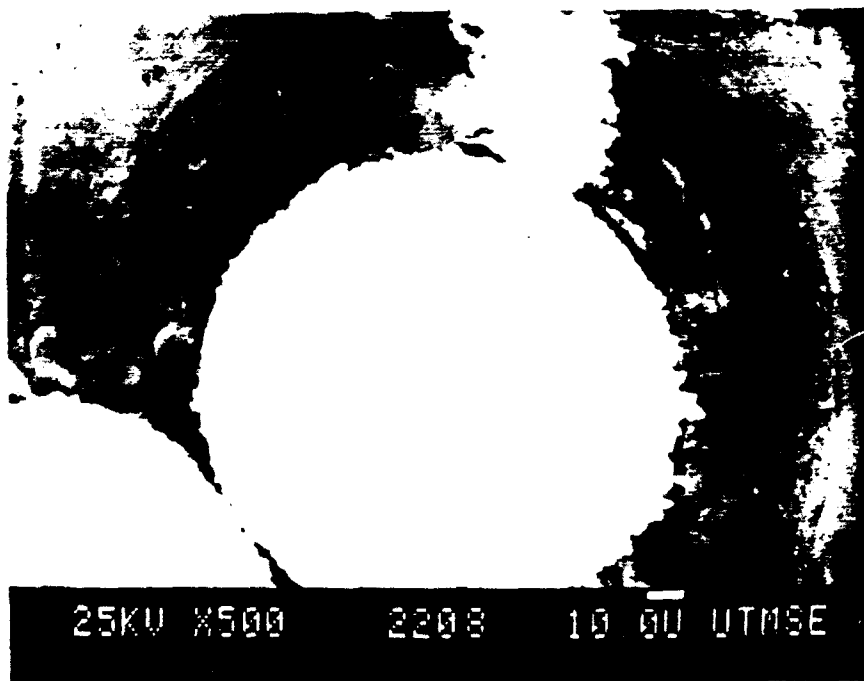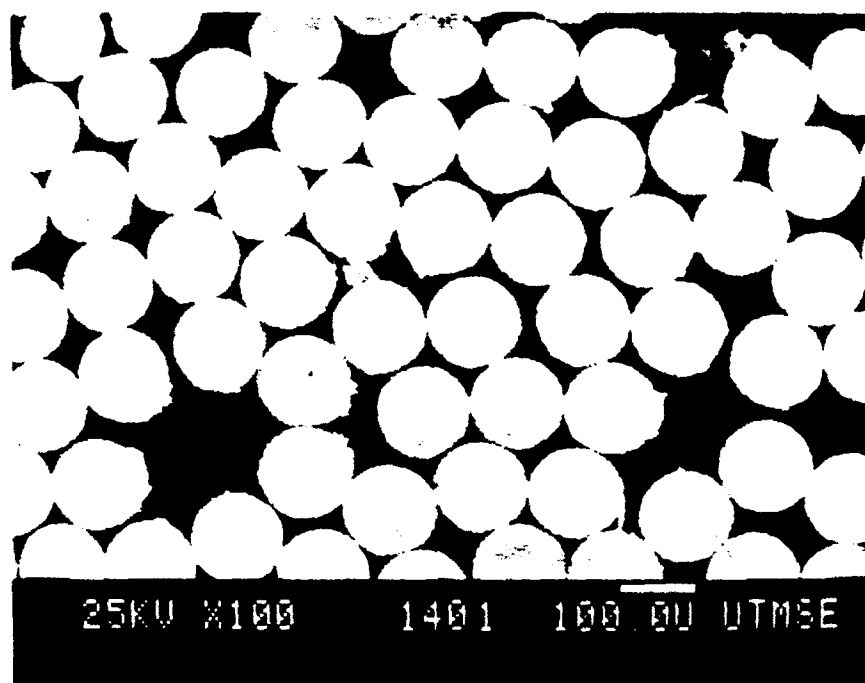
Figure 33a. SEM micrograph of a 70 vol % Wf Cu MMC after anodic polarization to 800 mV vs SCE in aerated 3.5 wt % NaCl.

Figure 33b. Higher magnification of composite in Figure 33a.
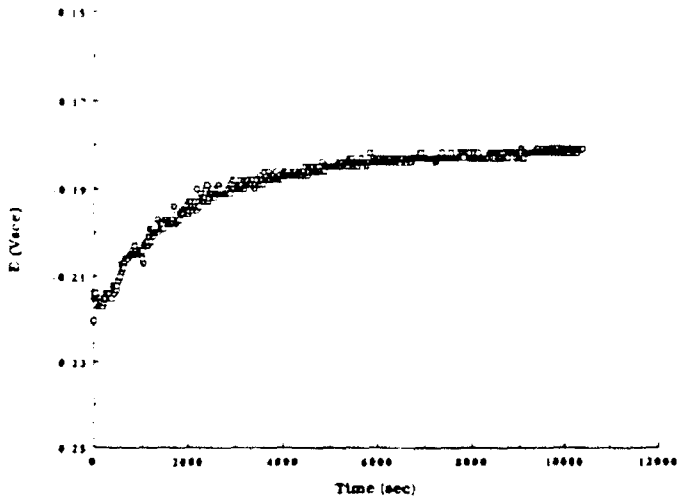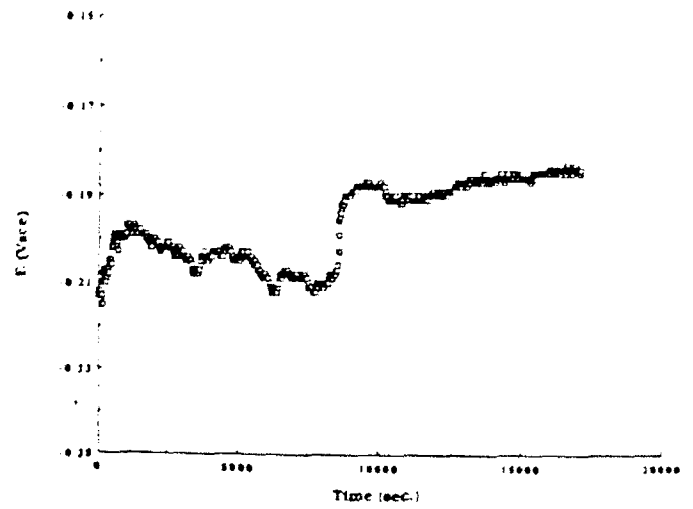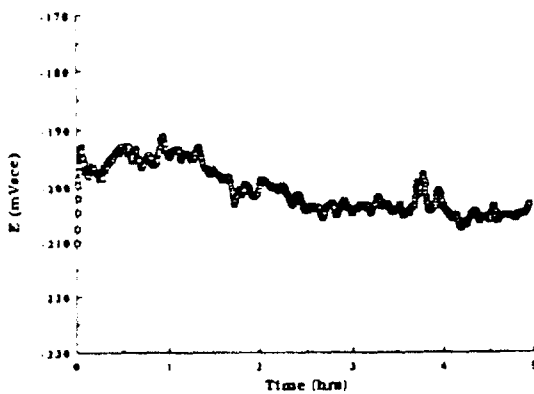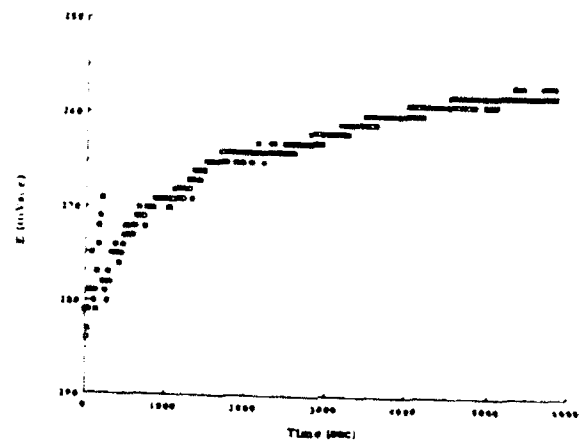
Figure 34a. E_{corr} vs time curve for HEHR 100% Copper in aerated 3.5 wt % NaCl + 200 ppm bezotriazole.

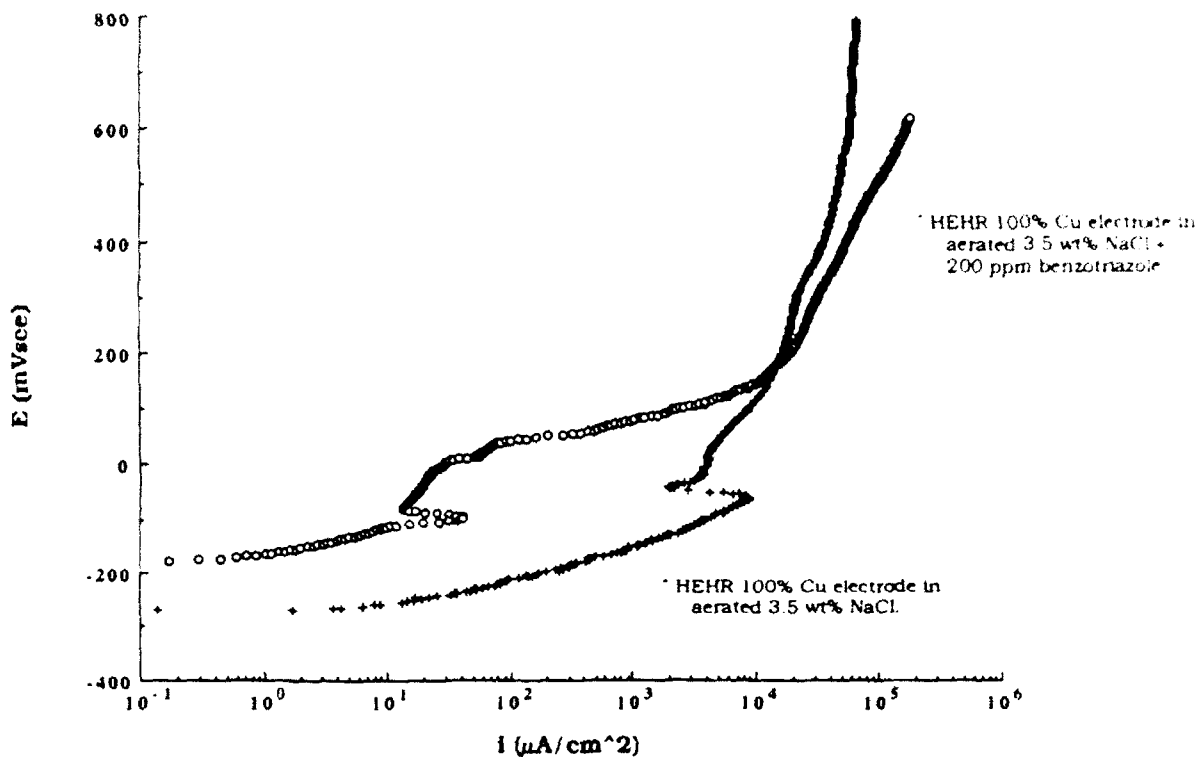Figure 34b. E_{corr} vs time curve for a 1.2 vol % Gr_p/Cu MMC in aerated 3.5 wt % NaCl + 200 ppm bezotriazole.

Figure 34c. E_{corr} vs time curve for a 50 vol % Gr_f/Cu MMC in aerated 3.5 wt % NaCl + 200 ppm bezotriazole.

Figure 34d. E_{corr} vs time curve for a 70 vol % W_f/Cu MMC in aerated 3.5 wt % NaCl + 200 ppm bezotriazole.

Figure 35. Typical anodic polarization curves for HEHR 100% Copper in aerated 3.5 wt % NaCl with and without 200 ppm bezotriazole.
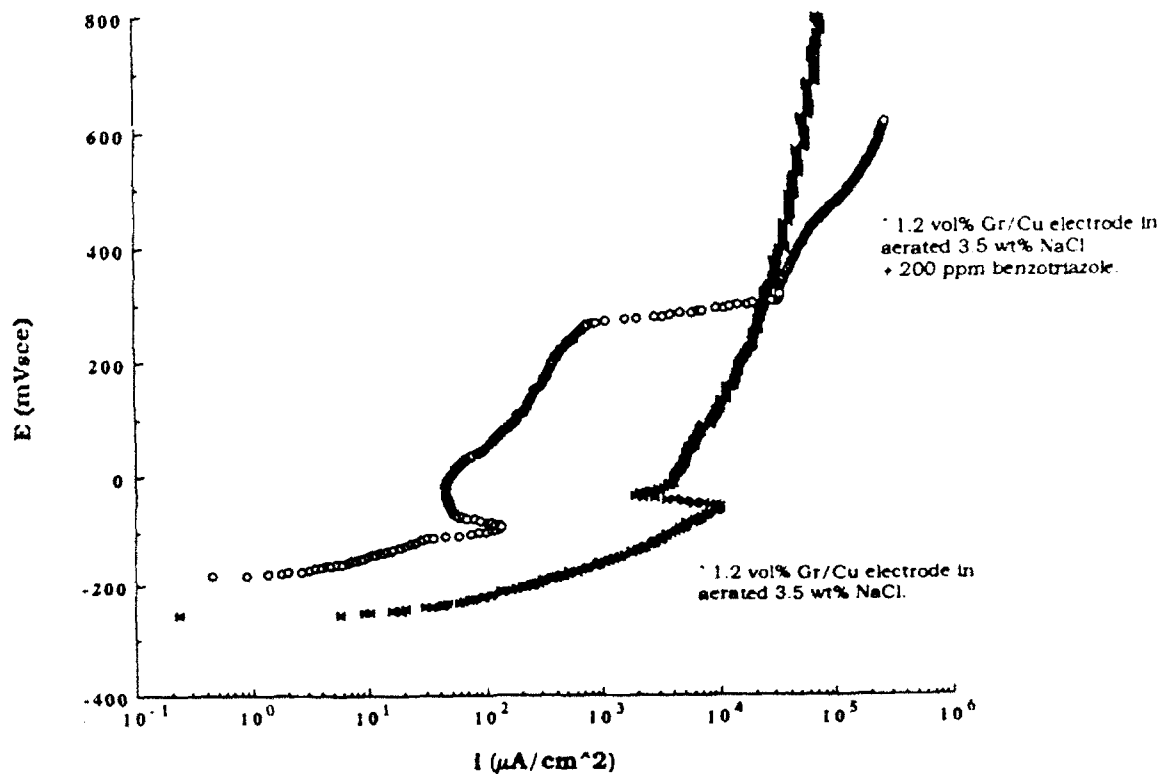
Figure 36. Typical anodic polarization curves for 1.2 vol % Gr$_p$/Cu MMCs in aerated 3.5 wt % NaCl with and without 200 ppm bezotriazole.
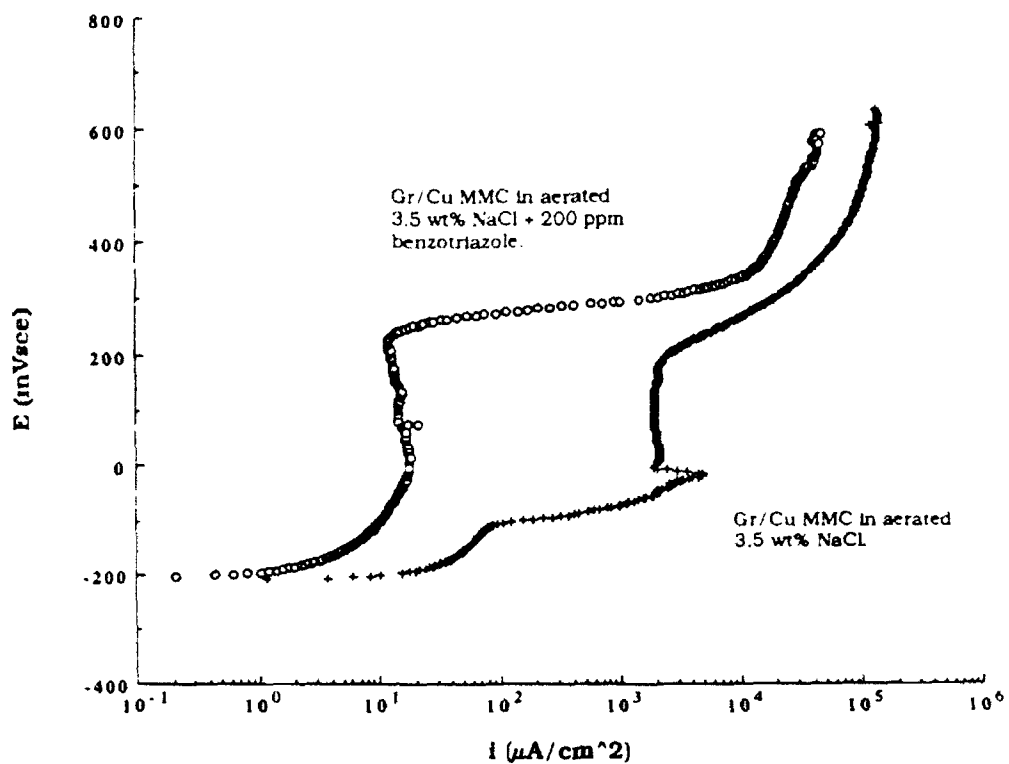
Figure 37. Typical polarization curves for a 50 vol % Gr$_f$/Cu MMC in aerated 3.5 wt % NaCl with and without 200 ppm bezotriazole.
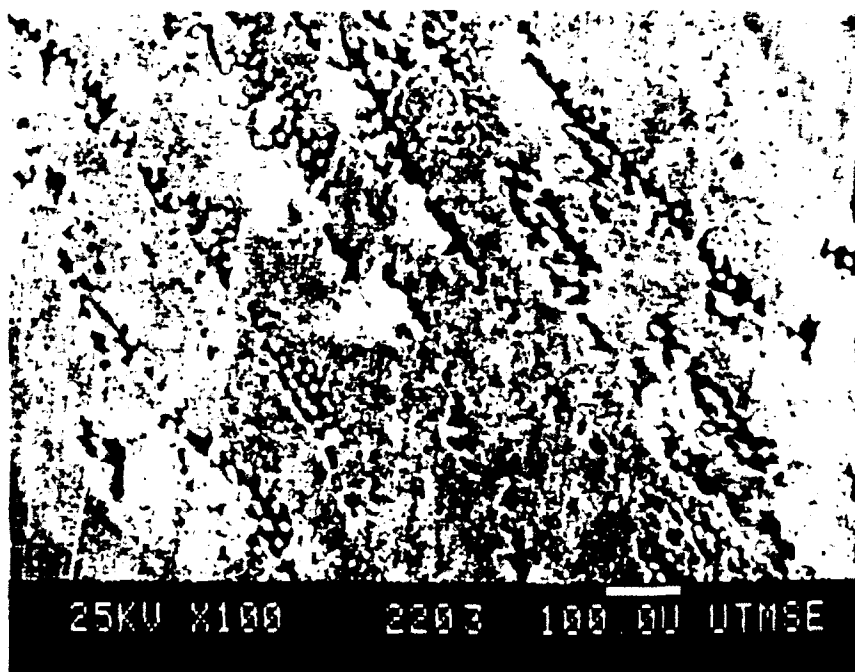

Figure 38. SEM micrograph of a 5C v% Gr$_f$/Cu MMC in aerated 3.5 wt % NaCl + 200 ppm bezotriazole. Specimen was polarized to 600 mV vs SCE.
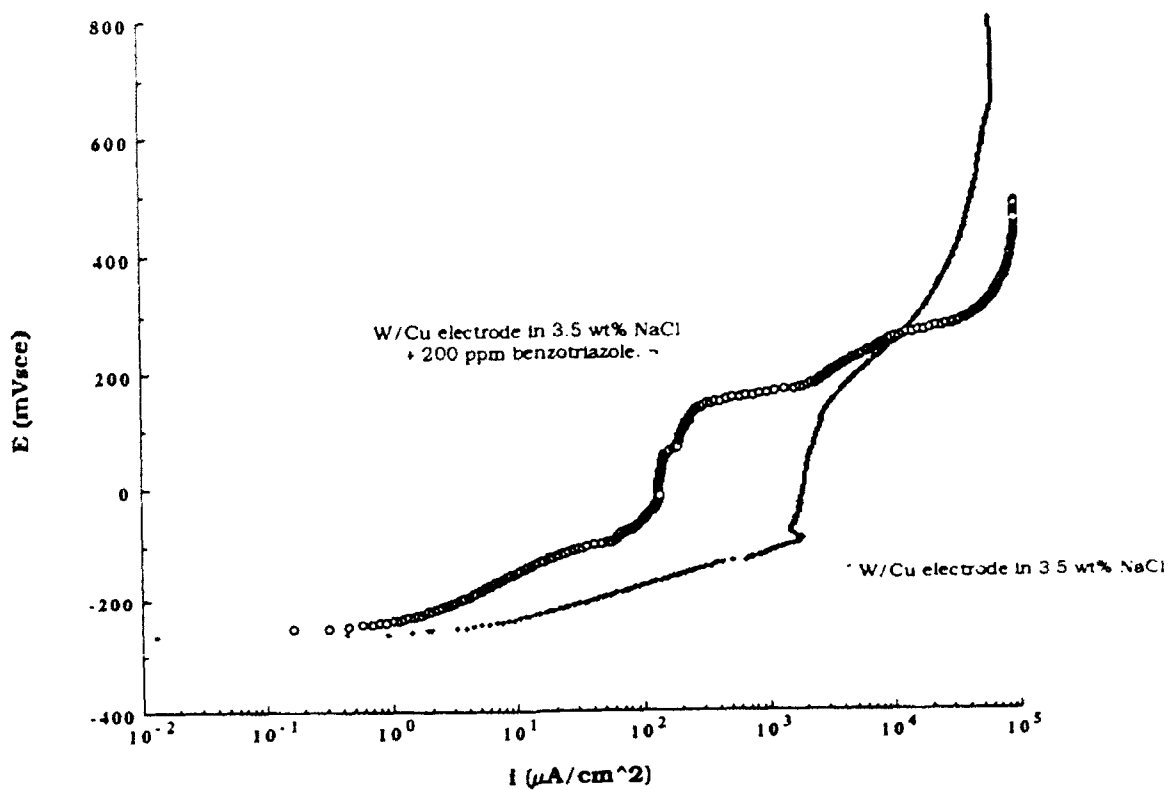
Figure 39. Typical polarization curves for a 70 vol % W_f/Cu MMC in aerated 3.5 w% NaCl + 200 ppm bezotriazole. (Scan rate was 0.2 mV/sec)
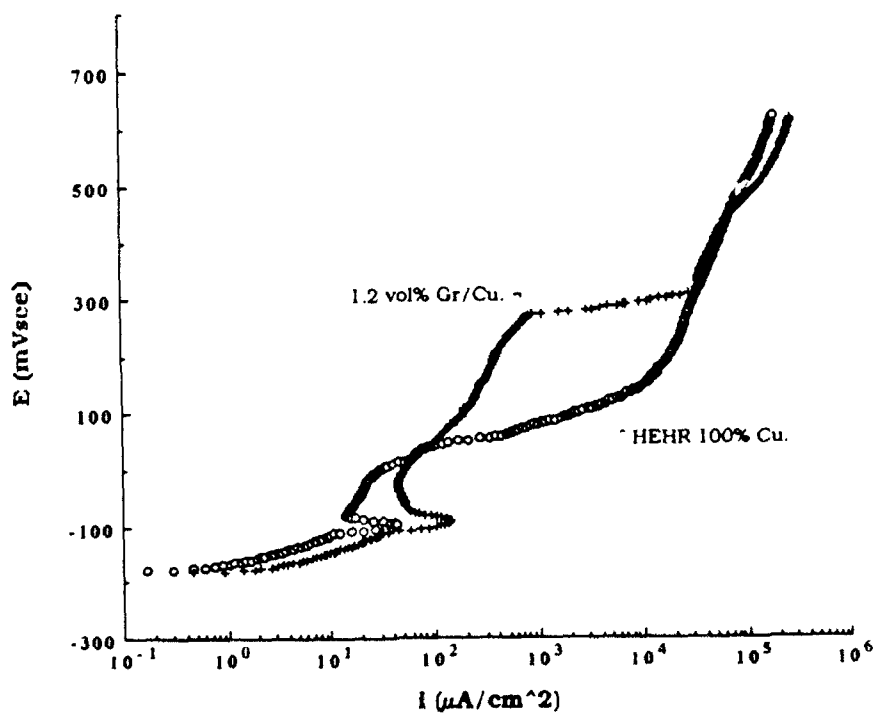

Figure 40. Anodic polarization curves comparing the electrochemical behavior of HEHR 100% Copper and a 1.2 vol % Gr_p/Cu MMC in aerated 3.5 wt % NaCl + 200 ppm bezotriazole. (Scan rates were 0.2 mV/sec)
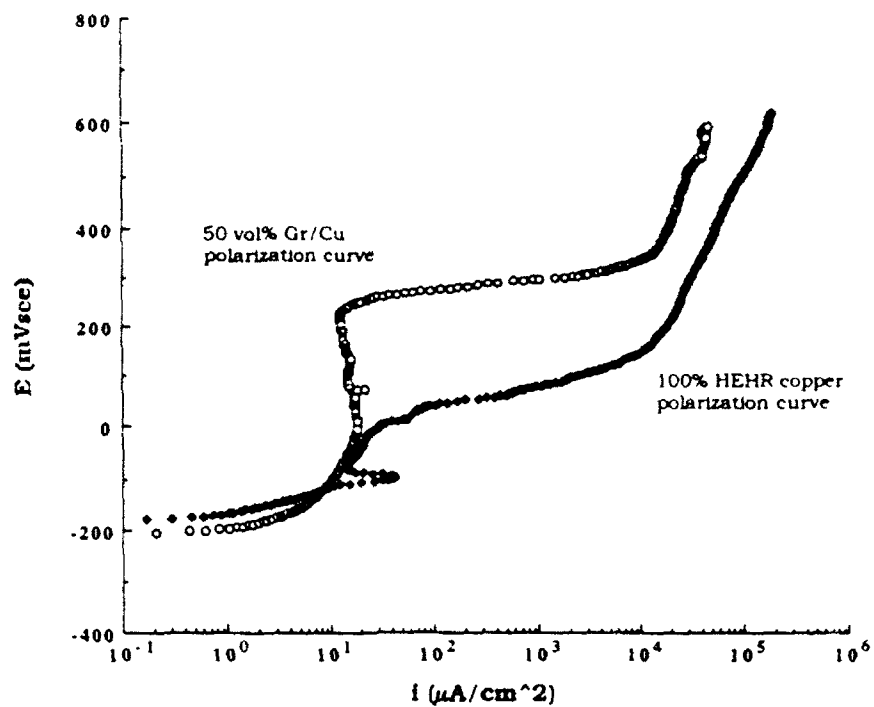
Figure 41. Anodic polarization curves comparing the electrochemical behavior of HEHR 100% Copper and a 50 vol % Gr_f/Cu MMC in aerated 3.5 wt % NaCl + 200 ppm bezotriazole. (Scan rates were 0.2 mV/sec)